energies

MDPI

Article

Effect of Individual Volt/var Control Strategies in *LINK*-Based Smart Grids with a High Photovoltaic Share

Daniel-Leon Schultis * and Albana Ilo

Institute of Energy Systems and Electrical Drives, TU Wien, 1040 Vienna, Austria; albana.ilo@tuwien.ac.at
* Correspondence: daniel-leon.schultis@tuwien.ac.at

Abstract: The increasing share of distributed energy resources aggravates voltage limit compliance within the electric power system. Nowadays, various inverter-based Volt/var control strategies, such as cos$\varphi(P)$ and $Q(U)$, for low voltage feeder connected $L(U)$ local control and on-load tap changers in distribution substations are investigated to mitigate the voltage limit violations caused by the extensive integration of rooftop photovoltaics. This study extends the $L(U)$ control strategy to $X(U)$ to also cover the case of a significant load increase, e.g., related to e-mobility. Control ensembles, including the reactive power autarky of customer plants, are also considered. All Volt/var control strategies are compared by conducting load flow calculations in a test distribution grid. For the first time, they are embedded into the *LINK*-based Volt/var chain scheme to provide a holistic view of their behavior and to facilitate systematic analysis. Their effect is assessed by calculating the voltage limit distortion and reactive power flows at different Link-Grid boundaries, the corresponding active power losses, and the distribution transformer loadings. The results show that the control ensemble $X(U)$ local control combined with reactive power self-sufficient customer plants performs better than the cos$\varphi(P)$ and $Q(U)$ local control strategies and the on-load tap changers in distribution substations.

Keywords: Volt/var control; distribution grid; photovoltaic; smart grid; *LINK*; boundary voltage limits; local control; $X(U)$; CP_Q-Autarky

check for updates

Citation: Schultis, D.-L.; Ilo, A. Effect of Individual Volt/var Control Strategies in *LINK*-Based Smart Grids with a High Photovoltaic Share. *Energies* **2021**, *14*, 5641. https://doi.org/10.3390/en14185641

Academic Editor: Luis Hernández-Callejo

Received: 18 August 2021
Accepted: 6 September 2021
Published: 8 September 2021

1. Introduction

Voltage is one of the basic quality parameters of power systems with limits specified in grid codes [1]. The massive connection of renewable and distributed generation and the increasing electricity demand aggravate compliance to the voltage limits, especially in the radial structures of distribution grids. Active and reactive power flows in these grids, as well as the transformers' tap positions, affect the voltages. However, active power is the only product of the power industry that, as a consequence, should not be used for voltage control, even in grids with an R/X ratio greater than 1. On the contrary, reactive power is a by-product of AC systems proven to have an essential effect on voltages. Therefore, controlling reactive power and on-load tap changers (OLTC) through a Volt/var control (VvC) process is feasible to maintain acceptable voltages within the distribution grid. Many distributed energy resources (DER) can participate in the VvC process by contributing reactive power [2]. Today, local controls are mainly used to utilize their var capabilities across all power system levels.

Rooftop photovoltaic (PV) inverters, installed at the customer plant (CP) level, are commonly equipped with cos$\varphi(P)$ and $Q(U)$ controls [3], or more sophisticated strategies [4–8], in order to mitigate voltage limit violations at the low voltage (LV) level. These control strategies may also be applied to electric vehicle (EV) chargers [9,10]. However, the distributed nature of CPs weakens the effectiveness of these control strategies [11], making active power curtailment necessary in many cases [12]. The use of customers' appliances to control the voltage in LV grids provokes social issues concerning data privacy and discrimination [13], contradicting the political intentions of the European Parliament [14,15]. As an alternative, local Volt/var control may be realized directly at the LV level. Some research projects have upgraded distribution transformers with OLTCs [16]. OLTCs are slow to operate and are sensitive to the number of tap operations. They cannot react appropriately to the voltage fluctuations caused by the intermittent PV injections. Temporary voltage limit violations and unnecessary tap operations are thus a consequence, jeopardizing the electrical equipment and shortening the transformers' durability [17]. Reference [18] proposes a Volt/var control ensemble, where $L(U)$ controlled inductive devices installed close to the ends of the violating LV feeders control the voltage locally, and the PV inverters supply the reactive power demand of the CPs. However, the increasing electricity demand, which is mainly due to the electrification of the heat and transportation sector [19], may provoke violations of the lower voltage limit that the inductive devices cannot mitigate. The OLTCs supplying substations control the voltage at the medium voltage (MV) level. In some cases, additional capacitor banks are used to support voltage control for long feeders [20].

The uncontrolled reactive power flows provoked by local VvCs in the radial structures of distributed grids constitute a significant concern for future smart grids [21]—transmission (TSO) and distribution system operators (DSO) are experiencing substantial operational challenges [22,23]. The use of modern information and communication technologies (ICT) to automatically optimize, protect, and monitor the operation of the complete power system, including CPs [24], does not meet the rigorous cyber-security and data privacy requirements [25].

Completing all technical and market-related aspects by meeting today's data protection and cyber security requirements requires a holistic view of smart grids [26]. The *LINK* architecture provides a holistic solution for smart grids, enabling the execution of various operation processes, such as demand response, static and dynamic stability, generation load balance, and monitoring [26,27]. It divides the power system into chains of grid-, producer-, and storage-links, which fit one into another to establish flexible and reliable electrical connections [28]. The standardized structure of *LINK*-based smart grids allows for realizing the Volt/var process in the horizontal and vertical axes as chain controls that minimize the necessary data exchanges [29]. While the horizontal axis includes the interconnected high voltage (HV) grids, the vertical ones contain all system levels, i.e., HV, MV, LV, and CP levels [30].

Numerous studies have been conducted to analyze the effects of different Volt/var control strategies on the behavior of LV grids using load flow simulations [13,31–34]. These studies calculate the grid state for a specified voltage at the slack node, but do not analyze the impact of Volt/var control on the boundary voltage limits (BVL) at the distribution and supplying substation levels [35] for different local control strategies such as $\cos\varphi(P)$, $Q(U)$, and OLTC in distribution transformers. This paper upgrades the $L(U)$ local control strategy to $X(U)$, supporting the increase in electricity demand, e.g., due to e-mobility. The *LINK* architecture [28] is used to analyze the impact of various Volt/var control strategies on the voltage limits at different system boundaries, such as LV−MV and MV−HV. All control setups are embedded into the *LINK*-based Volt/var control chain scheme.

Section 2 describes the materials and methods used, including the methodology, generalized Volt/var chain control, test grids, and control setups. The results are presented in Section 3. In Section 4, the effects of the different control setups are compared and discussed. Finally, conclusions are drawn in Section 5.

2. Materials and Methods

2.1. Methodology

2.1.1. Investigation Methodology

Figure 1 shows the methodology used to investigate the effects of the individual control strategies. The state-of-the-art and newly introduced local control strategies are embedded into the *LINK*-based Volt/var control process. Possible control ensembles, i.e., combinations of local controls at the LV level with the Q-Autarkic operation mode of customer plants, are identified. Load flow simulations are conducted in an exemplary vertical link chain, including the MV, LV, and CP levels, to quantify the effects of various control arrangements on the grid behavior.

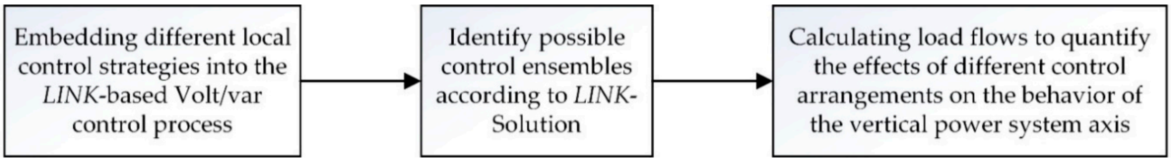

Figure 1. Methodology used to investigate the effects of individual control strategies in the *LINK*-based Volt/var control process.

2.1.2. Modeling Procedure

The *LINK*-based chain modeling procedure, introduced in [35] and overviewed in Figure 2, is used to calculate the test grids' behavior for different Volt/var control arrangements. In contrast with conventional load modeling, this approach uses the *BVL*-concept to validate voltage limit compliance throughout the entire Smart Grid through separate analysis of each system level. Joint modeling and analysis of MV and LV grids are not necessary. First, the lumped CP models are created by specifying their $P(U)$ and $Q(U)$ behavior and setting their boundary voltage limits to conform to the Grid Code. The lumped CP models are used to calculate the $P(U)$ and $Q(U)$ behavior and the boundary voltage limits at the distribution substation via load flow simulations, yielding the lumped LV grid models. Finally, load flow simulations are conducted at the MV level to identify the behavior and boundary voltage limits at the supplying substation. Their lumped models represent the connected LV grids and CPs. This calculation procedure is repeated for different Volt/var control arrangements to investigate their impact on the system behavior.

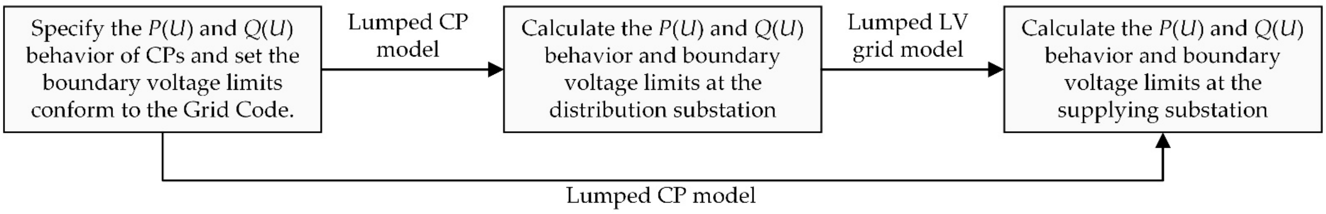

Figure 2. Overview of the *LINK*-based chain modeling procedure used to analyze the behavior of the test grids at distribution and supplying substations.

2.2. Generalized Vertical Volt/var Chain Control Scheme

LINK architecture arranges Volt/var chain control schemes in the horizontal and vertical power system axes. The focus of this study is set on the vertical Volt/var chain control scheme. It involves primary (PC), Direct (DiC), and secondary controls (SC) (see Appendix A) to maintain the voltage limit compliance throughout the entire smart grid by coordinating the reactive power flows with the on-load tap changers. Local controls (LC) may also be integrated.

Figure 3 shows the generalized form of the vertical Volt/var chain control wherein the grid-links are set according to HV, MV, LV, and CP levels. While the automation and communication path is drawn in blue, the power flow path is black. One of the evolutionary discoveries of the *LINK* solution is the grid identification within the customer plants and its consideration in the design of the holistic architecture [28]. The underpinned wires between the meter and the various sockets and electrical devices constitute a radial grid. The grid-link size is variable and is determined by the area where the corresponding SC is set up. It may be applied separately to each classical level of the grid and to a part that includes more than one level, e.g., MV and LV. Each grid-link includes electrical appliances, i.e., lines/cables, transformers, and reactive power devices (RPD); the Volt/var secondary control (Vv**SC**); and interfaces to the neighboring grid-, producer- and storage-links.

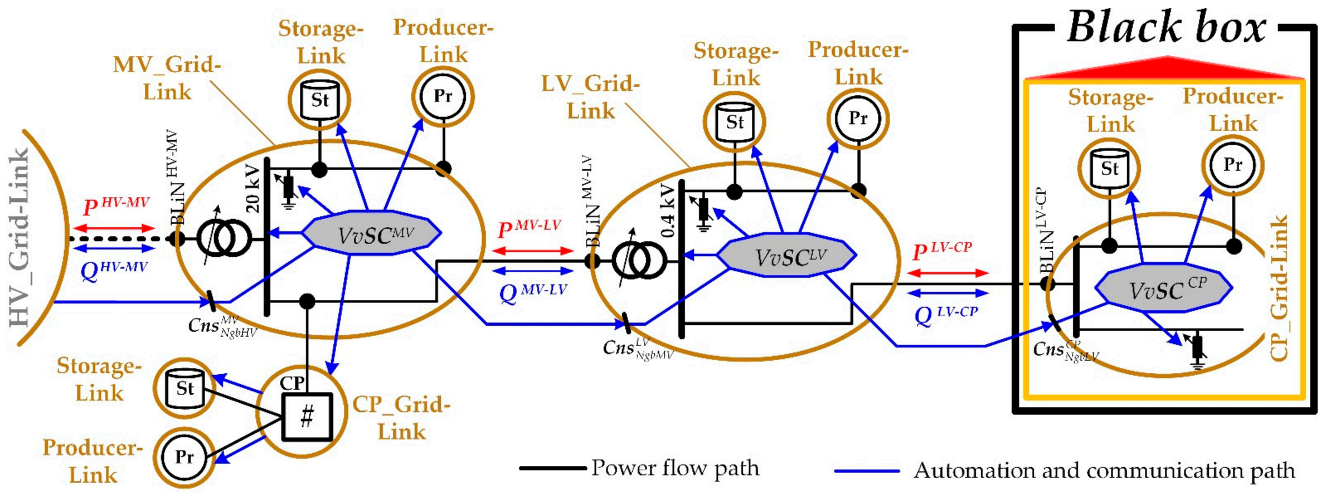

Figure 3. Overview of the generalized vertical Volt/var chain control.

The entirety of all electrical appliances included in a grid-link is denoted as the "Link-Grid". Link-Grids are interconnected via boundary link nodes (BLiN), and the producer- and storage-links are connected to the Link-Grids via boundary producer (BPN) and boundary storage nodes (BSN). Besides the electrical appliance, each producer- and storage-link includes a PC and an interface to the corresponding SC. In its generalized form, the Volt/var chain control utilizes all reactive power resources, including storages with reactive power capabilities, across all system levels. The neighboring grid-links may act as additional control variables by accepting reactive power set-points and considering them as constraints.

Equation (1) compactly represents the control variables and dynamic constraints of the vertical Volt/var chain control, considering the MV, LV, and CP levels. Three Vv**SC**s are involved that calculate the set-points for the corresponding control variables, which are put in parentheses.

$$Vv\boldsymbol{SC}_{chain}^{MV-LV-CP} = \Big\{ Vv\boldsymbol{SC}^{MV}\Big(\boldsymbol{PC}_{OLTC}^{MV}, \boldsymbol{PC}_{Pr}^{MV}, \boldsymbol{PC}_{St}^{MV}, \boldsymbol{PC}_{RPD}^{MV}, \boldsymbol{DiC}_{RPD}^{MV}, \boldsymbol{SC}_{NgbCP}^{MV}, \boldsymbol{SC}_{NgbLV}^{MV}; \boldsymbol{Cns}_{NgbHV}^{MV}\Big), \\ Vv\boldsymbol{SC}^{LV}\Big(\boldsymbol{PC}_{OLTC}^{LV}, \boldsymbol{PC}_{Pr}^{LV}, \boldsymbol{PC}_{St}^{LV}, \boldsymbol{PC}_{RPD}^{LV}, \boldsymbol{DiC}_{RPD}^{LV}, \boldsymbol{SC}_{NgbCP}^{LV}; \boldsymbol{Cns}_{NgbMV}^{LV}\Big), \\ Vv\boldsymbol{SC}^{CP}\Big(\boldsymbol{PC}_{Pr}^{CP}, \boldsymbol{PC}_{St}^{CP}, \boldsymbol{PC}_{RPD}^{CP}, \boldsymbol{DiC}_{RPD}^{CP}; \boldsymbol{Cns}_{NgbLV}^{CP}\Big)\Big\} \quad (1)$$

At the medium voltage level, $Vv\boldsymbol{SC}^{MV}$ calculates the following:

- The voltage set-points for the primary controls $\boldsymbol{PC}_{OLTC}^{MV}$ of the supplying transformers and other transformers included in the MV_Link-Grid that have OLTC;
- The voltage and reactive power set-points for the primary controls $\boldsymbol{PC}_{Pr}^{MV}$ of the producer-links connected to the MV_ Link-Grid;
- The voltage and reactive power set-points for the primary controls $\boldsymbol{PC}_{St}^{MV}$ of the storage-links connected to the MV_ Link-Grid;
- The voltage, reactive power, and switch position set-points for the primary $\boldsymbol{PC}_{RPD}^{MV}$ and direct controls $\boldsymbol{DiC}_{RPD}^{MV}$ of the RPDs included in the MV_ Link-Grid;
- The reactive power set-points for the secondary controls $\boldsymbol{SC}_{NgbCP}^{MV}$ of the neighboring CP_Grid-Links; and
- The reactive power set-points for the secondary controls $\boldsymbol{SC}_{NgbLV}^{MV}$ of the neighboring LV_Grid-Links;

While respecting the following:

- The reactive power constraint $\boldsymbol{Cns}_{NgbHV}^{MV}$ at the boundary node to the neighboring HV_ Link-Grid.

At the low voltage level, $Vv\boldsymbol{SC}^{LV}$ calculates the following:

- The voltage set-points for the primary control $\boldsymbol{PC}_{OLTC}^{LV}$ of the distribution transformer included in the LV_Link-Grid (when it possesses an OLTC);
- The voltage and reactive power set-points for the primary controls $\boldsymbol{PC}_{Pr}^{LV}$ of the producer-links connected to the LV_Link-Grid;
- The voltage and reactive power set-points for the primary controls $\boldsymbol{PC}_{St}^{LV}$ of the storage-links connected to the LV_Link-Grid;
- The voltage, reactive power, and switch position set-points for the primary $\boldsymbol{PC}_{RPD}^{LV}$ and direct controls $\boldsymbol{DiC}_{RPD}^{LV}$ of the RPDs included in the LV_Link-Grid; and
- The reactive power set-points for the secondary controls $\boldsymbol{SC}_{NgbCP}^{LV}$ of the neighboring CP_Grid-Links;

While respecting the following:

- The reactive power constraints $\boldsymbol{Cns}_{NgbMV}^{LV}$ at the boundary node to the neighboring MV_Link-Grid.

At the customer plant level, $Vv\boldsymbol{SC}^{CP}$ calculates the following:

- The voltage and reactive power set-points for the primary controls $\boldsymbol{PC}_{Pr}^{CP}$ of the producer-links connected to the CP_Link-Grid;
- The voltage and reactive power set-points for the primary controls $\boldsymbol{PC}_{St}^{CP}$ of the storage-links connected to the CP_Link-Grid; and
- The switch position set-points for the primary $\boldsymbol{PC}_{RPD}^{CP}$ and direct controls $\boldsymbol{DiC}_{RPD}^{CP}$ of the RPDs included in the CP_Link-Grid;

While respecting the following:

- The reactive power constraint $\boldsymbol{Cns}_{NgbLV}^{CP}$ at the boundary node to the neighboring LV_Link-Grid.

2.3. Description of Test Link-Grids

Figure 4a presents the structure of the test link chain. The MV_Link-Grid connects 15 hydroelectric power plants, 11 urban and 45 rural LV_Link-Grids, and 143 commercial and 2 industrial CP_Link-Grids. Meanwhile, the rural and urban LV grids supply 61 and 175 residential CPs, respectively. LV grids are considered balanced. The different Link-Grids are interconnected through the corresponding boundary link nodes (BLiN), i.e., the $\text{BLiN}^{\text{MV-LV}}$, $\text{BLiN}^{\text{MV-CP}}$, and $\text{BLiN}^{\text{LV-CP}}$. Meanwhile, the hydroelectric power plants are connected to the MV_Link-Grid through the BPN^{MV}. The HV level is not modeled, but the corresponding boundary link node is considered and denoted as $\text{BLiN}^{\text{HV-MV}}$.

2.3.1. Customer Plant Level

Four different types of CP_Link-Grids are considered: rural and urban residential, commercial, and industrial. Only the former is described in detail, while the others are documented in Appendix B. The voltage limits at the $\text{BLiN}^{\text{LV-CP}}$ are set to 0.9 and 1.1 p.u. and conform to the German Grid Code [36]. The corresponding active (P_t^{LV-CP}) and reactive power flows (Q_t^{LV-CP}) are determined by three model components: equivalent consuming device (Dev.-model), producer (Pr.-model), and storage model (St.-model; Figure 4b). The underpinned wires at the CP level are neglected. Figure 5 shows the load and production profiles of these model components, which have a resolution of 10 min.

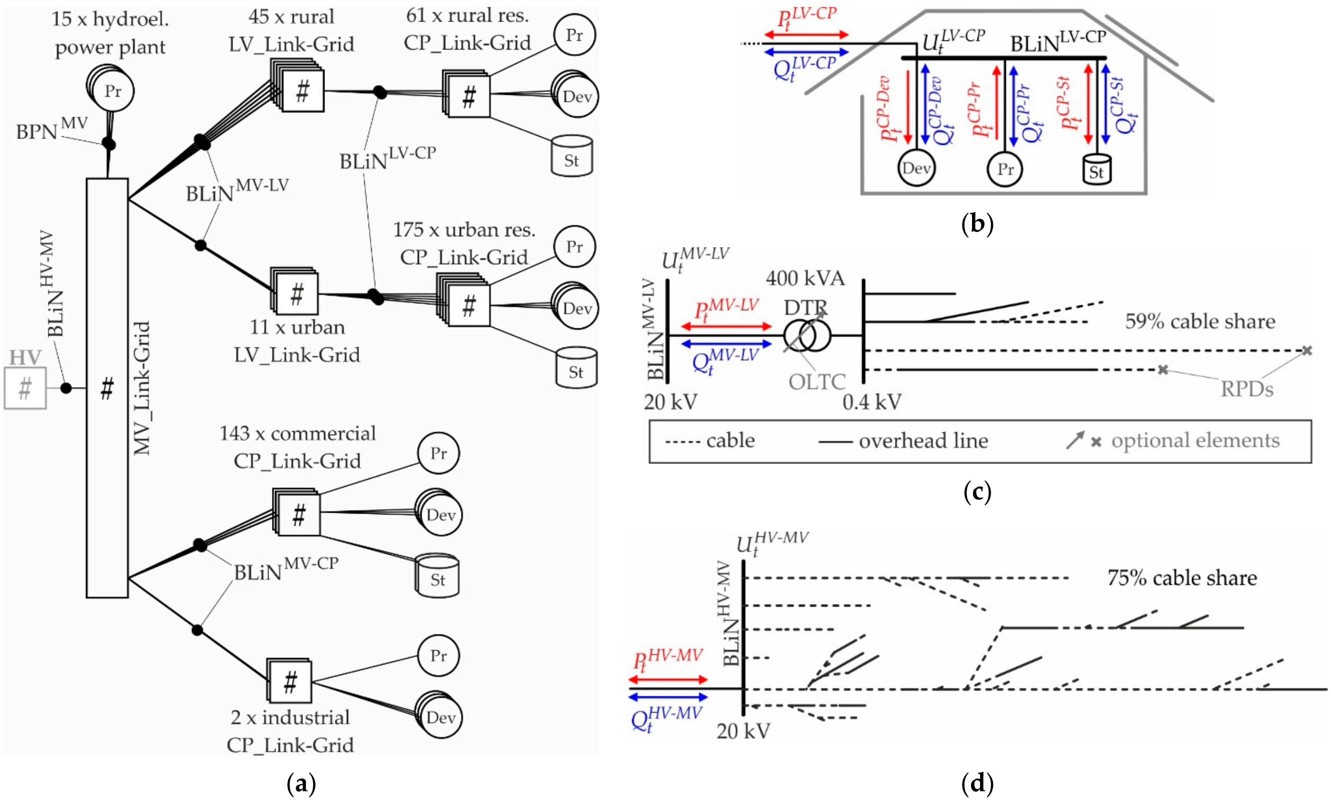

Figure 4. Structure of the test link chain: (**a**) overview; (**b**) residential CP_Link-Grids; (**c**) rural LV_Link-Grid; (**d**) MV_Link-Grid.

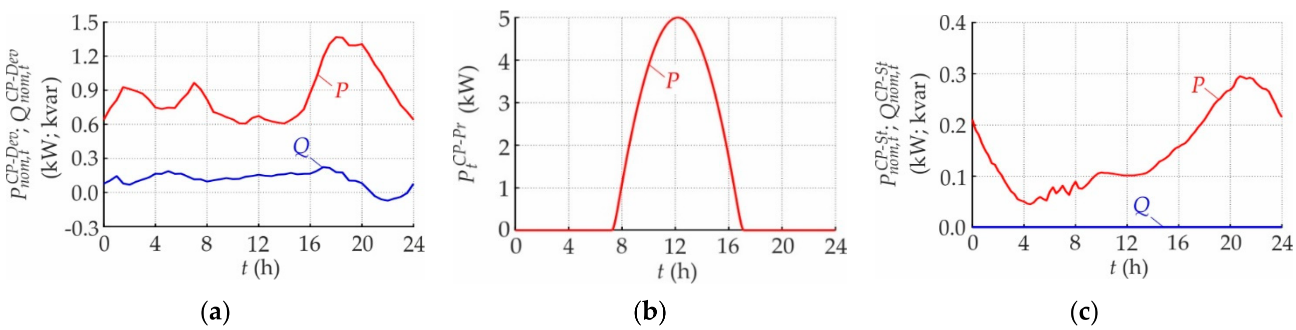

Figure 5. Load and production profiles of different model components of the rural residential CP_Link-Grid: (**a**) Dev.-model; (**b**) Pr.-model; (**c**) St.-model.

All consuming devices, such as switch-mode power supply, resistive, and lighting devices, as well as motors, are represented by the Dev.-model. Equation (2) determines the voltage-dependent active (P_t^{CP-Dev}) and reactive power contributions (Q_t^{CP-Dev}), using the load profiles and time-variant ZIP-coefficients from [37]. The load profiles reflect the time-dependency of consumption and depend on the behavior of the occupants and thermostatic controls that switch the consuming devices on and off. Figure 5a shows the load profiles used for the Dev.-model: they represent the consuming devices' average behavior over many CPs and consider modern equipment such as LED light bulbs. The latter provokes a capacitive behavior of residential CPs in the evening [38].

$$\begin{aligned} \frac{P_t^{CP-Dev}}{P_{nom,t}^{CP-Dev}} &= C_t^{Z,P} \cdot \left(\frac{U_t^{LV-CP}}{U_{nom}^{LV}} \right)^2 + C_t^{I,P} \cdot \left(\frac{U_t^{LV-CP}}{U_{nom}^{LV}} \right) + C_t^{P,P}, \\ \frac{Q_t^{CP-Dev}}{Q_{nom,t}^{CP-Dev}} &= C_t^{Z,Q} \cdot \left(\frac{U_t^{LV-CP}}{U_{nom}^{LV}} \right)^2 + C_t^{I,Q} \cdot \left(\frac{U_t^{LV-CP}}{U_{nom}^{LV}} \right) + C_t^{P,Q} \end{aligned} \tag{2}$$

where $C_t^{Z,P}$, $C_t^{I,P}$, $C_t^{P,P}$, and $C_t^{Z,Q}$, $C_t^{I,Q}$, $C_t^{P,Q}$ are the active and reactive power-related ZIP-coefficients; $P_{nom,t}^{CP-Dev}$ and $Q_{nom,t}^{CP-Dev}$ are the active and reactive power contributions of the Dev.-model for nominal voltage; U_t^{LV-CP} is the actual voltage at the $\text{BLiN}^{\text{LV-CP}}$; and U_{nom}^{LV} is the nominal voltage of the connecting LV_Link-Grid.

The PV system, which has module and inverter ratings of 5 kW and 5.56 kVA, respectively, is represented by the Pr.-model. The active power injection (P_t^{CP-Pr}) is voltage-independent [39] and follows the production profile shown in Figure 5b. The effects of clouds are not considered. The reactive power contribution (Q_t^{CP-Pr}) of the Pr.-model depends on the applied control arrangement (see Section 2.4).

An EV battery and the corresponding charger are represented by the St.-model. Through an analogy with the Dev.-model, the active power absorbed by the charger (P_t^{CP-St}) is specified using ZIP coefficients from [40] and load profiles from [41], using Equation (3). The load profiles, shown in Figure 5c, are identified based on measurements collected within the Low Carbon London EV trial and represent the average behavior of many residential EV chargers without any smart charging functionalities. The users initiate the charging processes by plugging in the EVs. The process is terminated when the battery is fully charged or prematurely disconnected from the charger. The St.-model's reactive power contribution is set to zero, i.e., their participation in the Volt/var process is not considered.

$$\frac{P_t^{CP-St}}{P_{nom,t}^{CP-St}} = -0.02\cdot\left(\frac{U_t^{LV-CP}}{U_{nom}^{LV}}\right)^2 + 0.03\cdot\left(\frac{U_t^{LV-CP}}{U_{nom}^{LV}}\right) + 0.99, \quad Q_t^{CP-St} = 0. \tag{3}$$

where $P_{nom,t}^{CP-St}$ is the active power consumption of the St.-model for nominal voltage at the $\text{BLiN}^{\text{LV-CP}}$.

2.3.2. Low Voltage Level

Two real Austrian LV grids are considered [42]: rural and urban. Therefore, only the rural one is described in detail. Figure 4c shows the main feeders of the rural LV_Link-Grid. The RPDs used for $X(U)$ in the local control (see Section 2.4.2) and the OLTC in the distribution substation are grey-colored as they are optional elements. The 0.4 kv grid includes four feeders with a 6.335 km total line length and 58.64% cable share. The shortest and longest feeders are 0.565 and 1.63 km in length, respectively. The 400 kVA distribution transformer (the real grid includes a DTR rated by 160 kVA [42]; a larger one is used in this study due to the high PV penetration set at the CP level) (DTR) with the transmission ratio of 21 kV/0.42 kV has a total short circuit voltage of 3.7%, whereby the resistive part amounts to 1%. Its OLTC has five tap positions, i.e., 1 to 5, and adds 2.5% of the nominal LV_Link-Grid voltage per tap. Tap position 3 is the mid position and sets the transmission ratio to its nominal value. The active ($P_t^{MV-\text{LV}}$) and reactive power ($Q_t^{MV-\text{LV}}$) flows at the DTR's primary side and corresponds to the $\text{BLiN}^{\text{MV-LV}}$.

2.3.3. Medium Voltage Level

Figure 4d shows the main feeders of a real Austrian 20 kV MV_Link-Grid. The STR is not included in the model, and therefore $\text{BLiN}^{\text{HV-MV}}$ corresponds to its secondary bus bar. The active and reactive power flows at these boundaries are denoted as $P_t^{HV-\text{MV}}$ and $Q_t^{HV-\text{MV}}$, respectively. The six MV feeders have a total length and cable share of 267.151 km and 74.66%, respectively. The shortest and longest feeders have lengths of 2 and 46.10 km, respectively. Hydroelectric power plants, rated between 60 and 400 kW, are modeled as PQ node-elements that constantly inject 70% of their peak generation; they do not contribute any reactive power. Conforming to the German Grid Code [36], voltage limits of 0.9 and 1.1 p.u. are considered at their BPNs.

2.4. Description of Volt/var Control Arrangements

Figure 6 overviews the investigated control arrangements according to the *LINK* architecture. Grid-links without Vv**SC** are shown in gold-colored dashed lines, as their existence should also be discussed in terms of load-generation balancing. The setups without any Volt/var control (Figure 6a), with cos$\varphi(P)$ and $Q(U)$ local controls at the CP level (Figure 6b), and with $X(U)$ (Figure 6c) and OLTC local controls at the LV levels (Figure 6d) are considered. The latter are also combined with Q-Autarkic CPs, forming control ensembles (Figure 6e,f). Analyzing the effect of Volt/var controls at the MV level is out of the scope of this paper as the hydroelectric power plants do not contribute any reactive power. The local controls at the CP level are applied only to the PV inverters but not to the EV chargers. However, excluding EV chargers from Volt/var control reduces the available inverter rating per CP, but does not affect the controls' functional principles. Therefore, no significant impact on the trends identified by comparing the control strategies is expected.

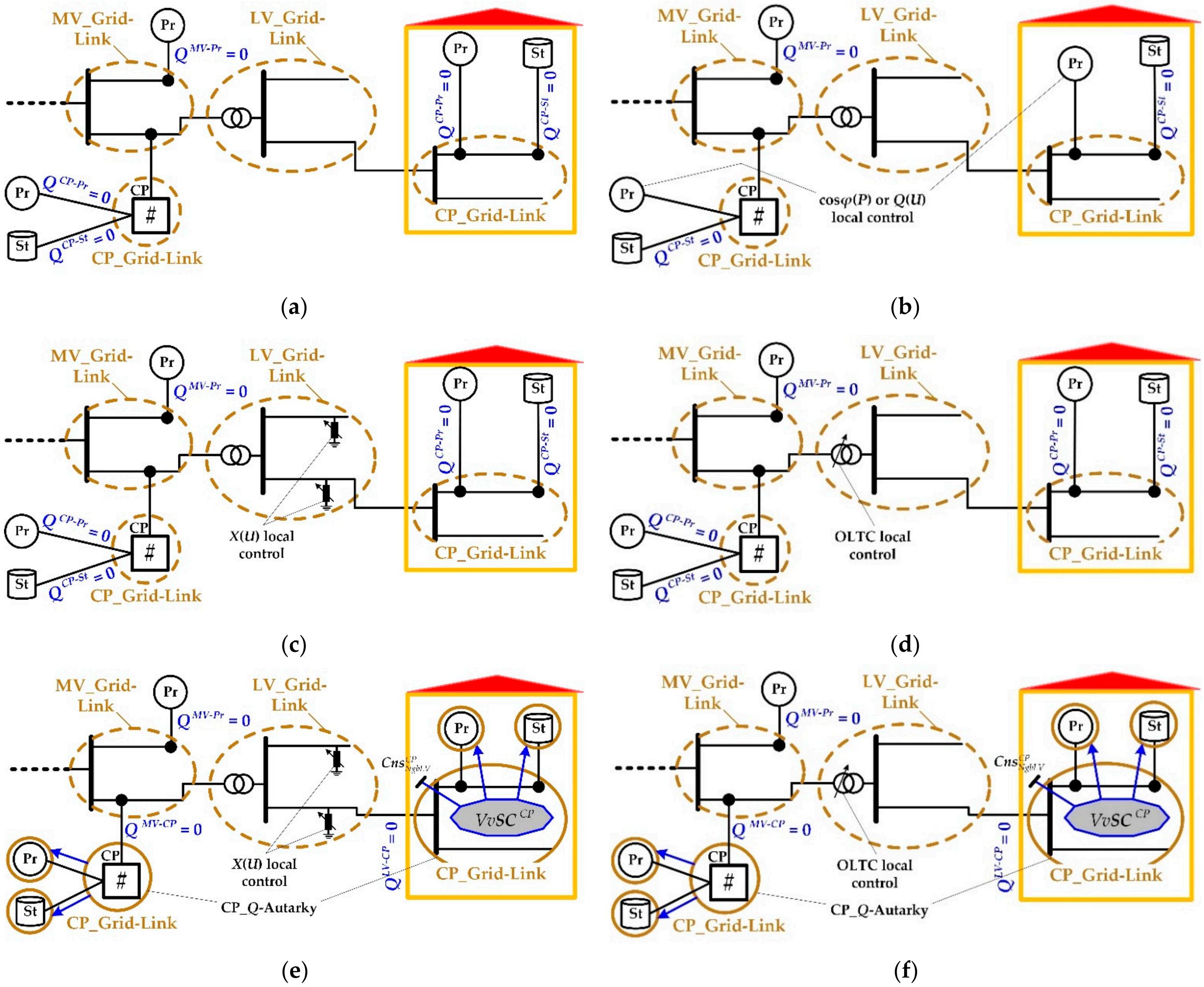

Figure 6. Overview of different Volt/var control arrangements: (**a**) no control; (**b**) cos$\varphi(P)$ or $Q(U)$ local control; (**c**) $X(U)$ local control; (**d**) OLTC local control; (**e**) $X(U)$ local control and CP_Q-Autarky; (**f**) OLTC local control and CP_Q-Autarky.

2.4.1. No Volt/var Control

Figure 6a shows the chain setup without any Volt/var control. No Vv**SC**s are involved, and all producers and storages inject or absorb active power with the unity power factor. No RPDs and OLTCs are considered: the tap changers of all DTRs are fixed in mid-position.

2.4.2. Local Controls

Local controls are used to mitigate the voltage limit violations by avoiding the need for any Vv**SC**s.

- cosφ(P) control at the CP level

Figure 6b shows the setup in which PV systems are upgraded with the cosφ(P) local control. No RPDs and OLTCs are considered: the tap changers of all DTRs are fixed in mid-position. Equation (4) compactly presents the resulting Volt/var control setup in the MV−LV−CP chain.

$$VvC^{MV-LV-CP} = \left\{ LC_{Pr}^{CP} = cos\varphi(P) \right\} \ or \ \left\{ LC_{Pr}^{CP} = Q(U) \right\} \quad (4)$$

Figure 7a shows the cosφ(P) control characteristic specified by the Austrian Grid Code [43] and used in all of the simulations. The inverters absorb reactive power when their active power injection (P^{CP-Pr}) exceeds a certain value, which is commonly set to 50% of the maximal active power production (P_{max}^{CP-Pr}). The inverters' power factors (cos φ^{CP-Pr}) are reduced from 1.0 down to 0.9 inductive in times of peak production.

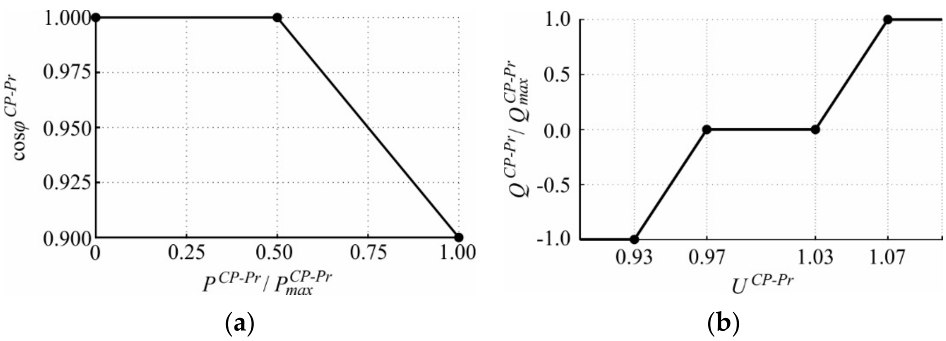

Figure 7. Different control characteristics for PV inverters: (**a**) cosφ(P); (**b**) $Q(U)$.

- $Q(U)$ local control at the CP level

Figure 6b and Equation (4) are also applied when PV systems are equipped with the $Q(U)$ local control. In this case, the PV inverters absorb the reactive power for high local voltages and inject reactive power for low ones. Figure 7b shows the default $Q(U)$ characteristic recommended by [44] and used in all of the simulations. The maximum reactive power contribution (Q_{max}^{CP-Pr}) depends on the inverter rating (S_r^{Pr}) and is set by Equation (5), conforming to the Austrian Grid Code [43], allowing for peak active power injection with a power factor of 0.9. No RPDs and OLTCs are considered: the tap changers of all DTRs are fixed in mid-position.

$$Q_{max}^{CP-Pr} = 0.436 \cdot S_r^{Pr} \quad (5)$$

- $X(U)$ local control at the LV level

Figure 6c shows the setup where RPDs equipped with the $X(U)$ local control are connected at selected LV feeders (see Figure 4c). The term "$X(U)$" refers to a voltage-dependent reactance that adjusts itself to maintain its terminal voltage within the acceptable range. In contrast with the $L(U)$ local control [18], which can only absorb reactive power, $X(U)$ can absorb and inject reactive power to mitigate violations of the upper and lower voltage limits. In practice, $X(U)$ is an inverter-based RPD connected close to the end of each violating feeder or branch (Figure 8). Here, it is parametrized to maintain the terminal voltage between 0.91 and 1.09 p.u.

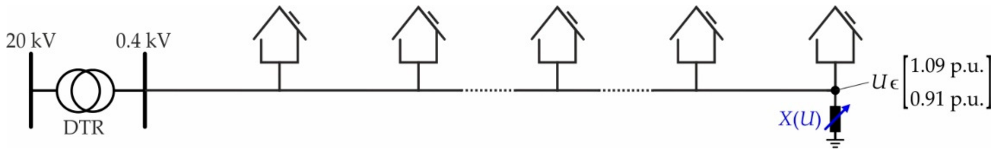

Figure 8. $X(U)$ local control strategy.

PV systems do not contribute any reactive power, and OLTCs are not considered: the tap changers of all DTRs are fixed in a mid-position. Equation (6) compactly presents the resulting Volt/var control setup in the MV−LV−CP chain.

$$VvC^{MV-LV-CP} = \left\{ \boldsymbol{LC}_{RPD}^{LV} \right\} \tag{6}$$

- OLTC local control at the LV level

Figure 6d shows the setup with the OLTC local control at the distribution substation. The OLTC in the distribution substation is locally controlled to maintain the voltage at the DTR's secondary bus within a predefined voltage band. Distinct voltage bands are specified for both LV_Link-Grids to maximally widen the voltage limits at the BLiN$^{\text{MV-LV}}$ for the investigated scenario. Table 1 lists the voltage ranges' lower (U_{min}) and upper limits (U_{max}) used in all of the simulations.

Table 1. Control parameters of the OLTC local control used for both test LV_Link-Grids.

LV_Link-Grid	U_{min}	U_{max}
Rural	0.950 p.u.	0.990 p.u.
Urban	0.950 p.u.	1.025 p.u.

No RPDs are considered, and PV systems do not contribute any reactive power. The resulting Volt/var control setup in the MV−LV−CP chain is presented in Equation (7).

$$VvC^{MV-LV-CP} = \left\{ \boldsymbol{LC}_{OLTC}^{LV} \right\} \tag{7}$$

2.4.3. Control Ensembles

The $X(U)$ and OLTC local controls may be combined with the Q-Autarky of customer plants [18]. The latter does not intend to control the voltage but supplies the customers' reactive power demand locally. Vv**SC**s are set up only at the CP level, and the corresponding producers and storages are upgraded with primary controls.

- $X(U)$ local control at the LV level and Q-Autarky at the CP level

Figure 6e shows the setup where the $X(U)$ local control is combined with CP_Q-Autarky. To realize CP_Q-Autarky, the $Vv\boldsymbol{SC}^{CP}$ adapts the primary control settings of the corresponding producer- and storage-Links to eliminate the reactive power flow through the BLiN$^{\text{LV-CP}}$ at all times. RPDs equipped with the $X(U)$ local control are connected at selected LV feeders (see Section 2.4.2). OLTCs are not considered: the tap changers of all DTRs are fixed in mid-position. Equation (8) compactly presents the resulting Volt/var control setup.

$$VvC^{MV-LV-CP} = \left\{ \boldsymbol{LC}_{RPD}^{LV},\ Vv\boldsymbol{SC}^{CP}\left(\boldsymbol{PC}_{Pr}^{CP},\ \boldsymbol{PC}_{St}^{CP}; \boldsymbol{Cns}_{NgbLV}^{CP} = 0\ \text{kvar} \right) \right\} \tag{8}$$

- OLTC local control at the LV level and Q-Autarky at the CP level

Figure 6f shows the setup where the OLTC local control is combined with Q-Autarkic CPs. The CPs do not exchange any reactive power with the LV and MV grids. DTRs are upgraded with OLTC local controls (see Section 2.4.2), and no RPDs are considered. The resulting Volt/var control setup is presented in Equation (9).

$$VvC^{MV-LV-CP} = \left\{ \boldsymbol{LC}_{OLTC}^{LV},\ Vv\boldsymbol{SC}^{CP}\left(\boldsymbol{PC}_{Pr}^{CP},\ \boldsymbol{PC}_{St}^{CP}; \boldsymbol{Cns}_{NgbLV}^{CP} = 0\,\text{kvar} \right) \right\} \tag{9}$$

3. Link-Grid Behavior under Different Volt/var Control Arrangements

This section discusses the behavior of the test link chain at different system boundaries by computing the load flows for the Volt/var control arrangements presented in Section 2.4. Therefore, the $P(U)$ and $Q(U)$ behavior and the voltage limits are calculated at the MV−LV and HV−MV boundaries. The grid losses, DTR loadings, and power flows over system boundaries are discussed in detail for the cases listed in Table 2. The active power flows are analyzed exclusively for the setup without any Volt/var control, because the different control strategies only slightly modify it. Depending on the viewpoint, the boundary voltage may apply to the HV−MV or MV−LV boundary node. The behavior at the MV−LV boundary is discussed only for the rural LV_Link-Grid, as the same trends are observed in the urban one.

Table 2. Voltage−time-pairs of the test cases discussed in detail.

Case	Boundary Voltage	Daytime
I	1.05 p.u.	06:00
II	0.95 p.u.	12:10
$\widetilde{\text{II}}$	1.00 p.u.	12:10
III	1.00 p.u.	22:10

3.1. No Control

The voltage behavior, active and reactive power exchanges, active power losses, and DTR loadings of the test link chain without any Volt/var control are discussed.

3.1.1. Voltage Behavior

Figure 9 shows the voltage limits at different boundaries of the test link chain. As shown by the straight lines, the Grid Code fixes $BVL^{LV\text{-}CP}$, which correspond to the customer plants' delivery points, at 0.9 and 1.1 p.u. Meanwhile, as the dashed and dotted lines indicate, curved voltage limits ($BVL^{MV\text{-}LV}$ and $BVL^{HV\text{-}MV}$) occur at the MV−LV and HV−MV boundaries. Any violation of these limits results in violations of the legally stipulated voltage limits at the delivery points of CPs and hydropower plants.

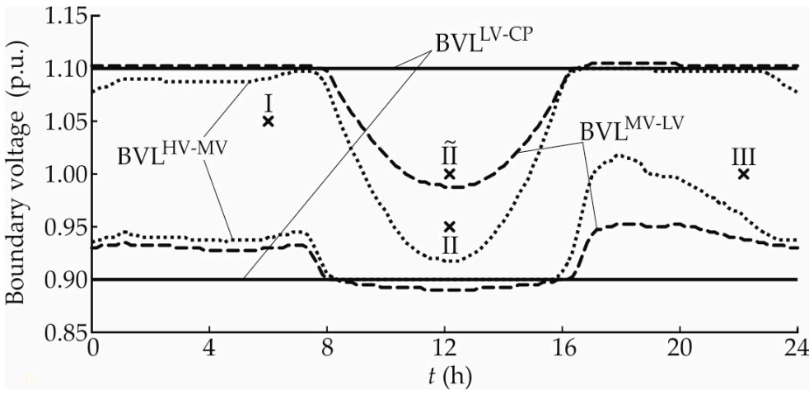

Figure 9. Voltage limits at the LV−CP (rural residential CP_Link-Grid), MV−LV (rural LV_Link-Grid), and HV−MV boundaries when no Volt/var control is applied.

The PV production strongly tightens the upper $BVL^{MV\text{-}LV}$ and $BVL^{HV\text{-}MV}$, reaching very low values of 0.9875 and 0.9175 p.u., respectively, at around noon-time. Around midday, limit violations occur for HV−MV and MV−LV boundary voltages of 0.95 (case II) and 1 p.u. (case $\widetilde{\text{II}}$), respectively. The lower limits are tighten before 08:00 a.m. and after 16:15 p.m., i.e., when no significant PV injection is present. The lower $BVL^{MV\text{-}LV}$ and $BVL^{HV\text{-}MV}$ reach 0.9525 and 1.0175 p.u., respectively, in the evening hours. The results clearly show that the test link chain can hardly be operated without additional measures.

The LV feeders' voltage profiles are shown in Figure 10a,b for cases II and $\widetilde{\text{II}}$, respectively. The upper LV−CP boundary voltage limit at 12:10 p.m. ($\overline{BVL}_{12:10}^{LV-CP}$) is indicated by a dashed black line. While the boundary link nodes to the rural residential CP_Link-Grids are marked as black dots, the BLiN$^{\text{MV-LV}}$ is highlighted as a grey cross. The PV injections considerably raise the feeder voltages, provoking upper limit violations in case $\widetilde{\text{II}}$ (Figure 10b).

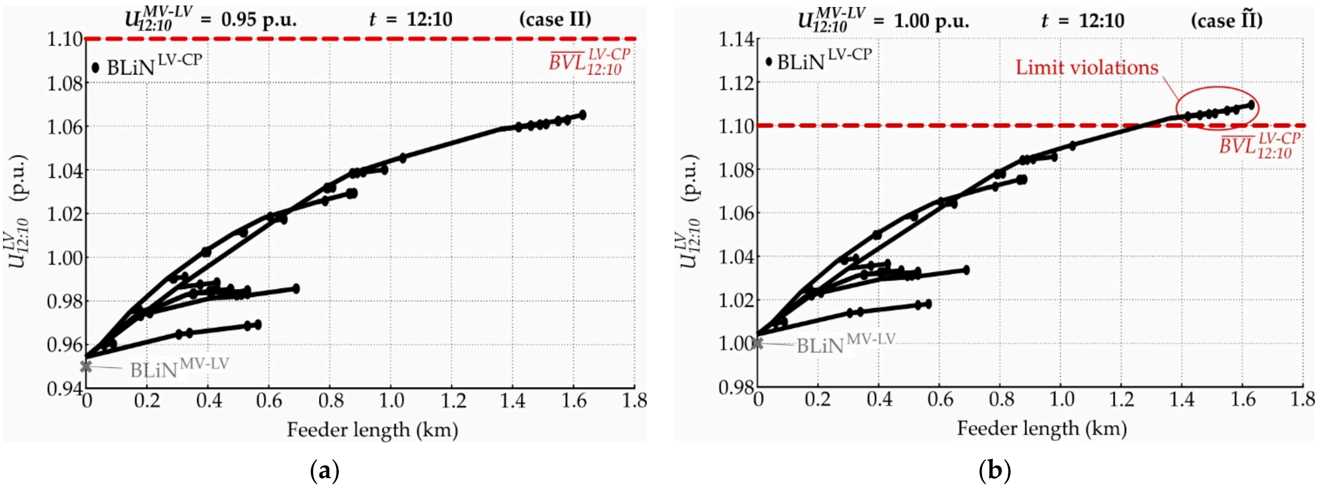

Figure 10. Voltage profiles of the rural LV_Link-Grid's feeders without any Volt/var control at 12:10 p.m. for different MV−LV boundary voltages: (**a**) 0.95 p.u. (case II); (**b**) 1.00 p.u. (case $\widetilde{\text{II}}$).

Figure 11 shows the MV feeders' voltage profiles for case II. Black bullets and red asterisks indicate the connection points of CP_Link-Grids and hydroelectric power plants, respectively. Meanwhile, connection points of urban and rural LV_Link-Grids are highlighted as violet and yellow asterisks, respectively.

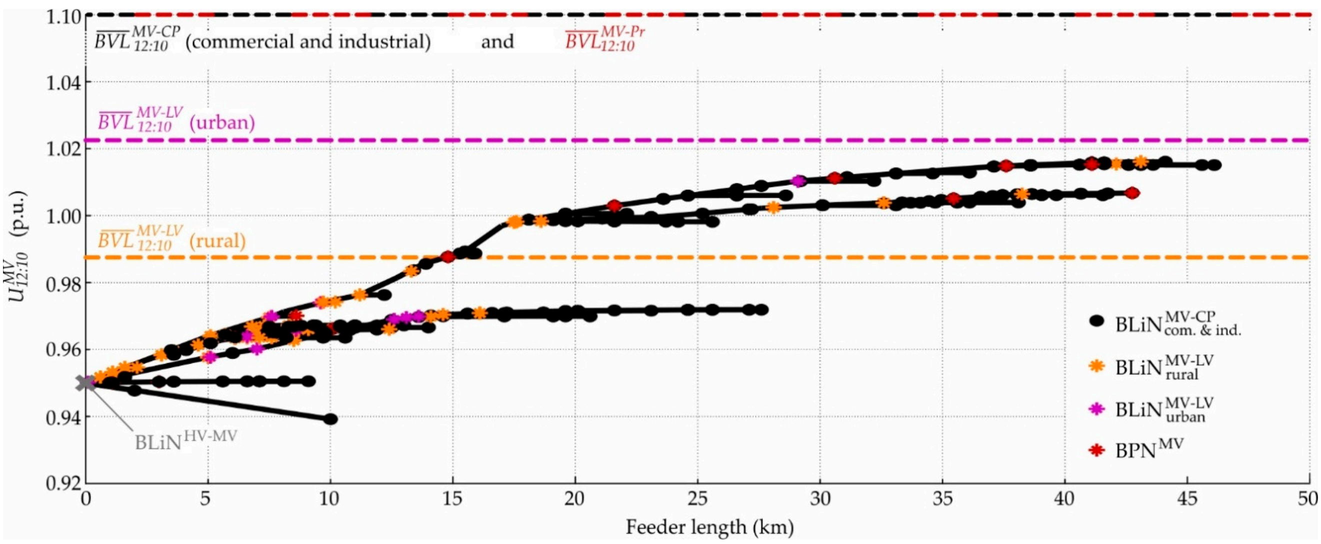

Figure 11. MV feeders' voltage profiles in case II.

Dashed lines in the same colors represent the upper *BVL*s. Conforming to the Grid Code, an upper voltage limit of $\overline{BVL}_t^{MV-CP} = \overline{BVL}_t^{MV-Pr} = 1.1$ p.u. prevails at the connection points of CP_Link-Grids and power plants. At 12:10 p.m., maximal voltages of 1.0225 and 0.9875 p.u. are acceptable at the $BLiN^{MV\text{-}LV}$ of the urban and rural LV_Link-Grid, respectively (see Figure 9 for the rural one). The voltages increase up to 1.0161 p.u., provoking upper limit violations for some $BLiN^{MV\text{-}LV}$ to the rural LV_Link-Grid. Consequently, case II lies within the upper limit violation zone. Figure 11 also shows that no LV_Link-Grids are connected to two relatively short MV feeders. This should be kept in mind when comparing the different Volt/var control strategies: in contrast with the PV inverter-based controls, the $X(U)$ and OLTC local controls do not affect the voltage profiles of these two MV feeders.

3.1.2. Active Power Exchange

Figure 12 shows the active power exchange over different system boundaries for various boundary voltages and no Volt/var control.

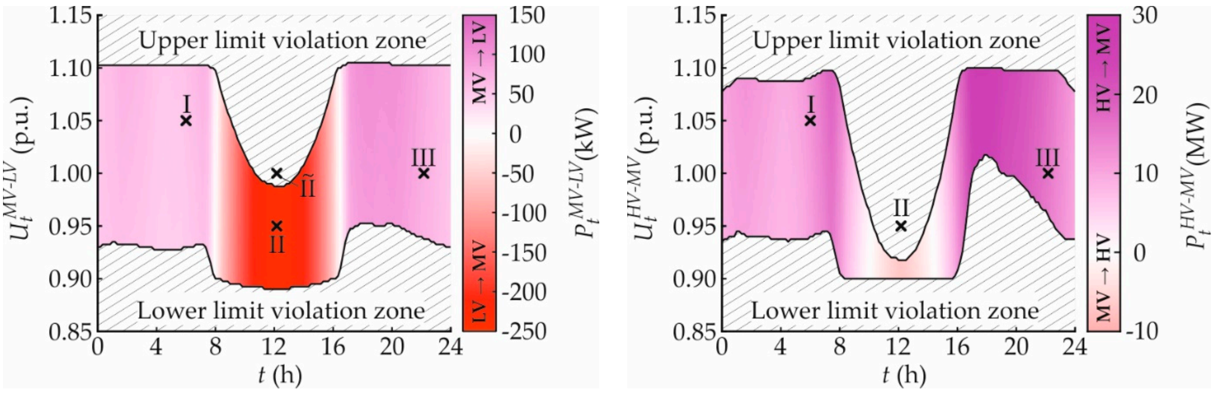

Figure 12. Daily active power exchange over different system boundaries for various boundary voltages and no Volt/var control: (**a**) MV−LV boundary (rural LV_Link-Grid); (**b**) HV−MV boundary.

The daytime and the corresponding boundary voltage are plotted on the abscissa and ordinate, respectively. Meanwhile, the active power exchange is presented in the relevant zone, i.e., between the upper and lower *BVL*s, using different color shades from red for the upstream flows (LV→MV and MV→HV) to violet for the downstream ones. The active power flows through both regarded boundaries are characterized by an intense time- and a weak voltage-dependency. Flow direction changes twice a day.

From 00:00 a.m. to 08:00 a.m., the LV_Link-Grid draws active power from the MV level, consuming 56.62 kW in case I (Figure 12a). When the total PV production exceeds the total consumption, i.e., from 08:00 a.m. to 16:15 p.m., the active power flow reverses, reaching its maximum at 12:10 p.m. At this time, 241.99 kW is injected into the MV level in case II. When consumption exceeds production, i.e., from 16:15 p.m. to 00:00 a.m., the active power changes its direction again and flows from the MV into the LV_Link-Grid. In case III, the LV_Link-Grid consumes 73.85 kW. Between 10:15 a.m. and 13:59 p.m., active power flows from the MV into the HV level, while before and afterwards, it flows in reverse (Figure 12b). In cases I and III, 12.22 and 15.21 MW are absorbed by the MV_Link-Grid, respectively, while in case II, 6.22 MW flows into the HV level.

3.1.3. Reactive Power Exchange

Figure 13 shows the reactive power exchange over different system boundaries for various boundary voltages and no Volt/var control. It is presented in the relevant zone using different color shades from blue for upstream flows (LV→MV and MV→HV) to cyan for downstream ones. The reactive power behavior is characterized by a significant time- and a slight voltage-dependency and changes its flow direction twice a day.

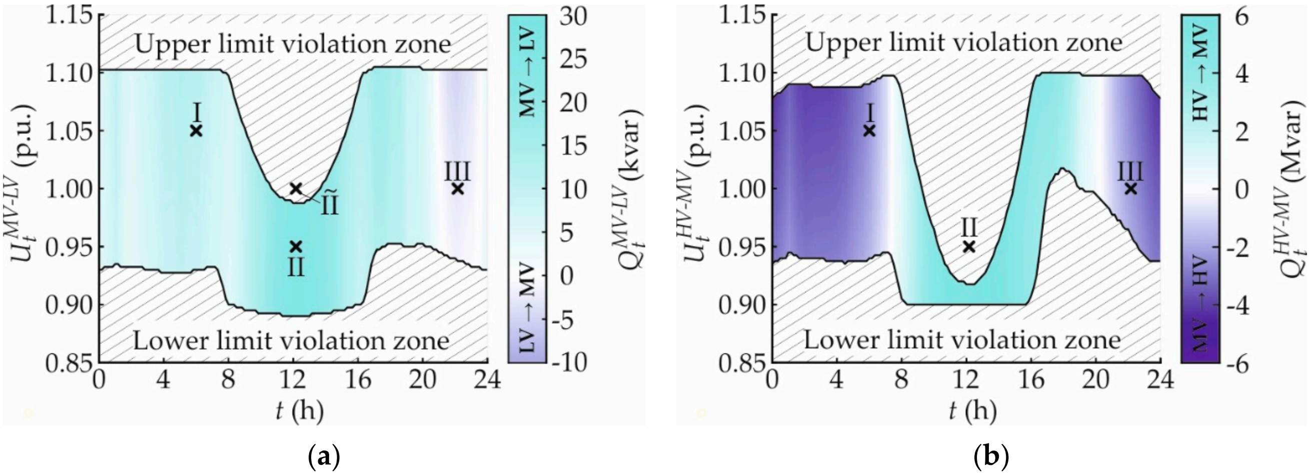

Figure 13. Daily reactive power exchange over different system boundaries for various boundary voltages and no Volt/var control: (**a**) MV−LV boundary (rural LV_Link-Grid); (**b**) HV−MV boundary.

Figure 13a shows that the reactive power flows from the MV into the LV_Link-Grid from 00:00 a.m. to 20:45 p.m., reaching 11.21 and 24.78 kvar in cases I and II, respectively. Later on, the reactive power flow reverses until 23:30 p.m. due to the capacitive behavior of modern consuming devices (mainly LED light bulbs). In case III, 2.53 kvar flows into the MV level.

MV→HV reactive power flows occur before 07:19 a.m. and after 20:12 p.m., reaching 2.18 and 2.29 Mvar in cases I and III, respectively. In case II, a reverse flow of 5.32 Mvar occurs.

3.1.4. Active Power Loss

Figure 14 shows the daily active power loss (ΔP_t^{LV} and ΔP_t^{MV}) within different system levels for various boundary voltages and no Volt/var control. It is presented in the relevant zone using different color shades, from violet for high losses to white for zero losses. The considerable time- and a weak voltage-dependency of the active and reactive power exchanges also characterize the active power loss. Figure 14a shows the daily active power loss of the rural LV_Link-Grid, including line and transformer losses. Intensive losses occur during PV production periods, reaching 0.76, 15.97, and 1.39 kW in cases I, II, and III, respectively. As shown in Figure 14b, relatively high active power losses occur at the MV level around midday and around 18:00 p.m. For cases I, II, and III, 83.11, 536.98, and 144.18 kW are lost respectively.

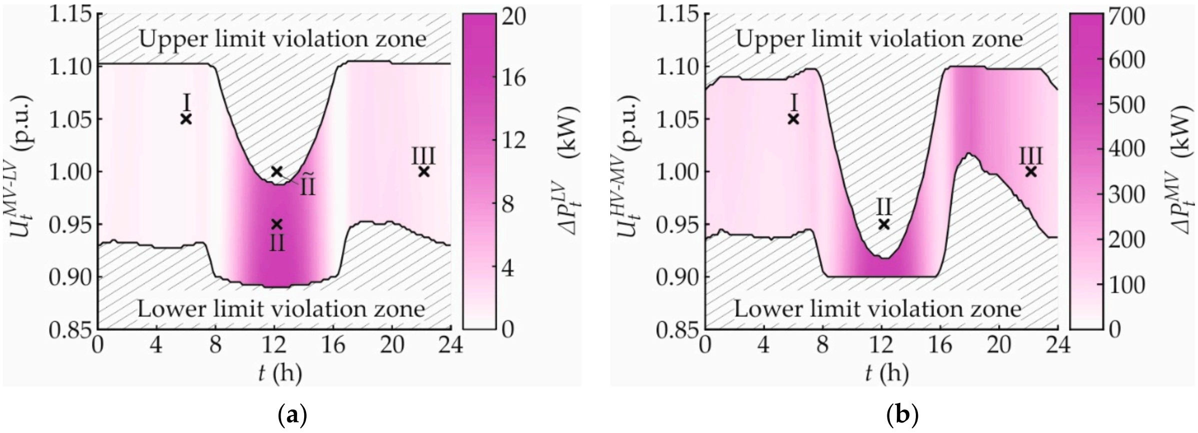

Figure 14. Daily active power loss within different system levels for various boundary voltages and no Volt/var control: (**a**) LV level (rural LV_Link-Grid); (**b**) MV level.

3.1.5. Distribution Transformer Loading

Figure 15 shows the daily distribution transformer loading ($Loading_t^{DTR}$) within the rural LV_Link-Grid for various boundary voltages and no Volt/var control. Black indicates a loading of 80% while white stands for zero loading. The strong time-dependency of power flows provokes a strong-time dependency of the DTR loading. Values of 13.74, 64.01, and 18.47% are calculated for cases I, II, and III, respectively.

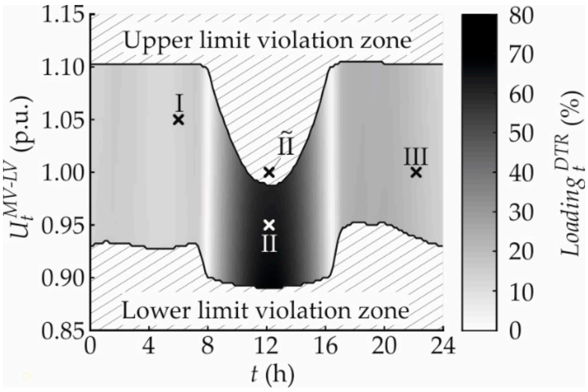

Figure 15. Daily distribution transformer loading within the rural LV_Link-Grid for various MV−LV boundary voltages and no Volt/var control.

3.2. Local Controls

3.2.1. cosφ(P)

Figure 16 shows the daily behavior of the test link chain for various boundary voltages and the cosφ(P) local control. The boundary voltage limits arising from the setup without any Volt/var control are indicated by dotted lines. The cosφ(P) local control is active during times of significant PV production, modifying the boundary voltage limits, reactive power flows, losses, and DTR loading in the corresponding intervals. Between 08:53 a.m. and 15:28 p.m., the upper $BVL^{MV\text{-}LV}$ is significantly widened, and the lower one is slightly tightened. At the same time, both $BVL^{HV\text{-}MV}$ are increased: the upper one is relaxed at midday to 1.0025, i.e., by 0.085 p.u., but the lower one remains highly restrictive around 18:00 p.m.

Figure 16a,b shows that the cosφ(P) local control excessively increases the reactive power exchanges through the MV−LV and HV−MV boundaries during the day, reaching 179.62 kvar and 21.19 Mvar, respectively, in case II. In addition, the losses are drastically increased during the day. In case II, 23.92 and 846.09 kW are lost within the LV and MV levels, respectively (Figure 16c,d). The DRT loading, shown in Figure 16e, is increased during times of significant PV production, reaching 77.96% in case II.

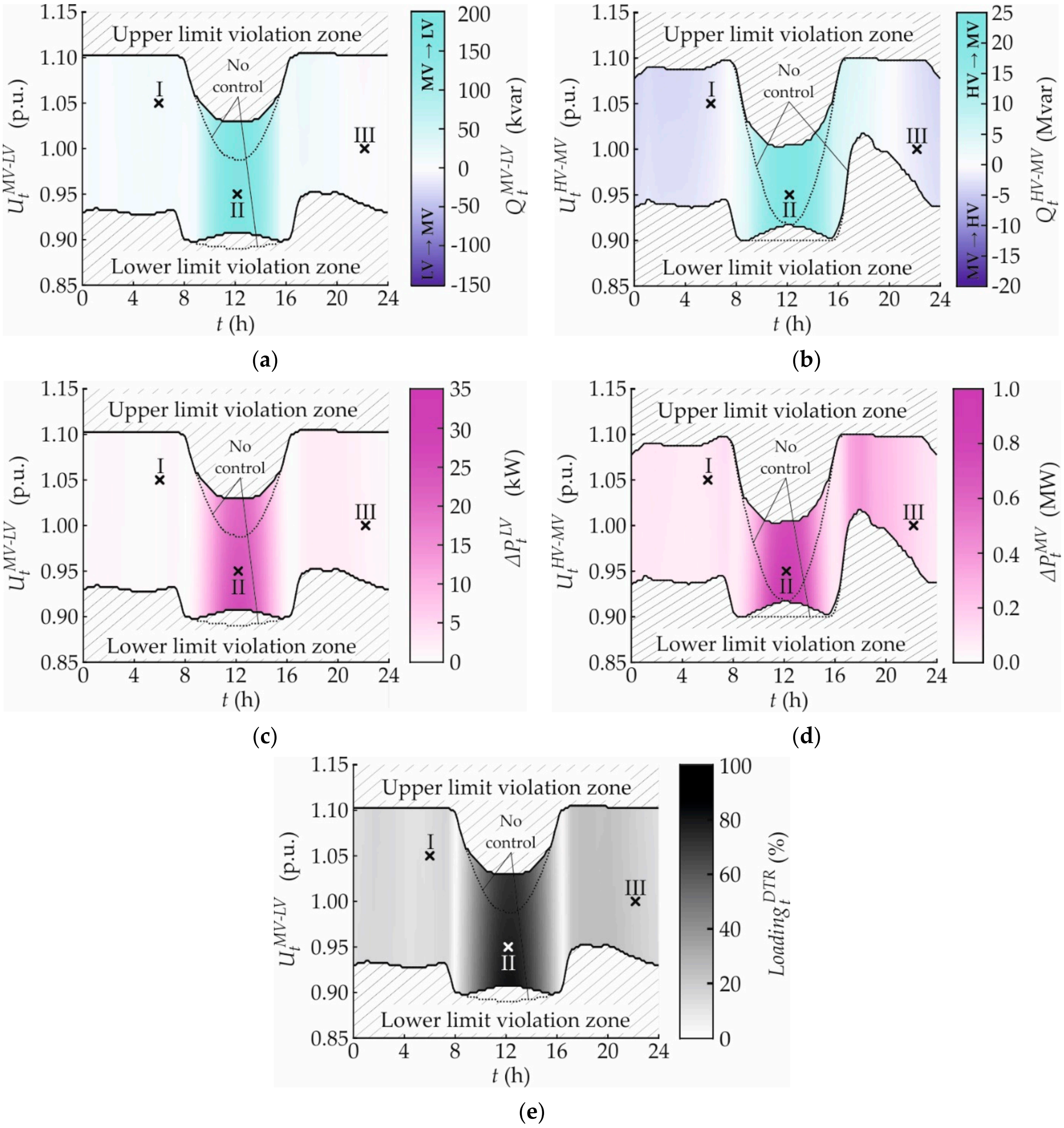

Figure 16. Daily behavior of the test link chain for various boundary voltages and the cosφ(P) local control: (**a**) reactive power exchange over the MV−LV boundary (rural LV_Link-Grid); (**b**) reactive power exchange over the HV−MV boundary; (**c**) active power loss within the rural LV_Link-Grid; (**d**) active power loss within the MV_Link-Grid; (**e**) DTR loading (rural LV_Link-Grid).

3.2.2. $Q(U)$

Figure 17 shows the daily behavior of the test link chain for various boundary voltages and the $Q(U)$ local control. The $Q(U)$ local control is active throughout the whole day for wide ranges of boundary voltage, even when no voltage support is necessary. It compresses both limit violation zones, allowing for MV−LV boundary voltages above 1.1 and below 0.9 p.u. many hours a day. At midday, the upper $BVL^{MV\text{-}LV}$ and $BVL^{HV\text{-}MV}$ of 1.0225 and 0.965 p.u. remain relatively restrictive. Meanwhile, the lower ones are considerably relaxed, reaching 0.9125 and 0.9425 p.u., respectively, at 18:00 p.m.

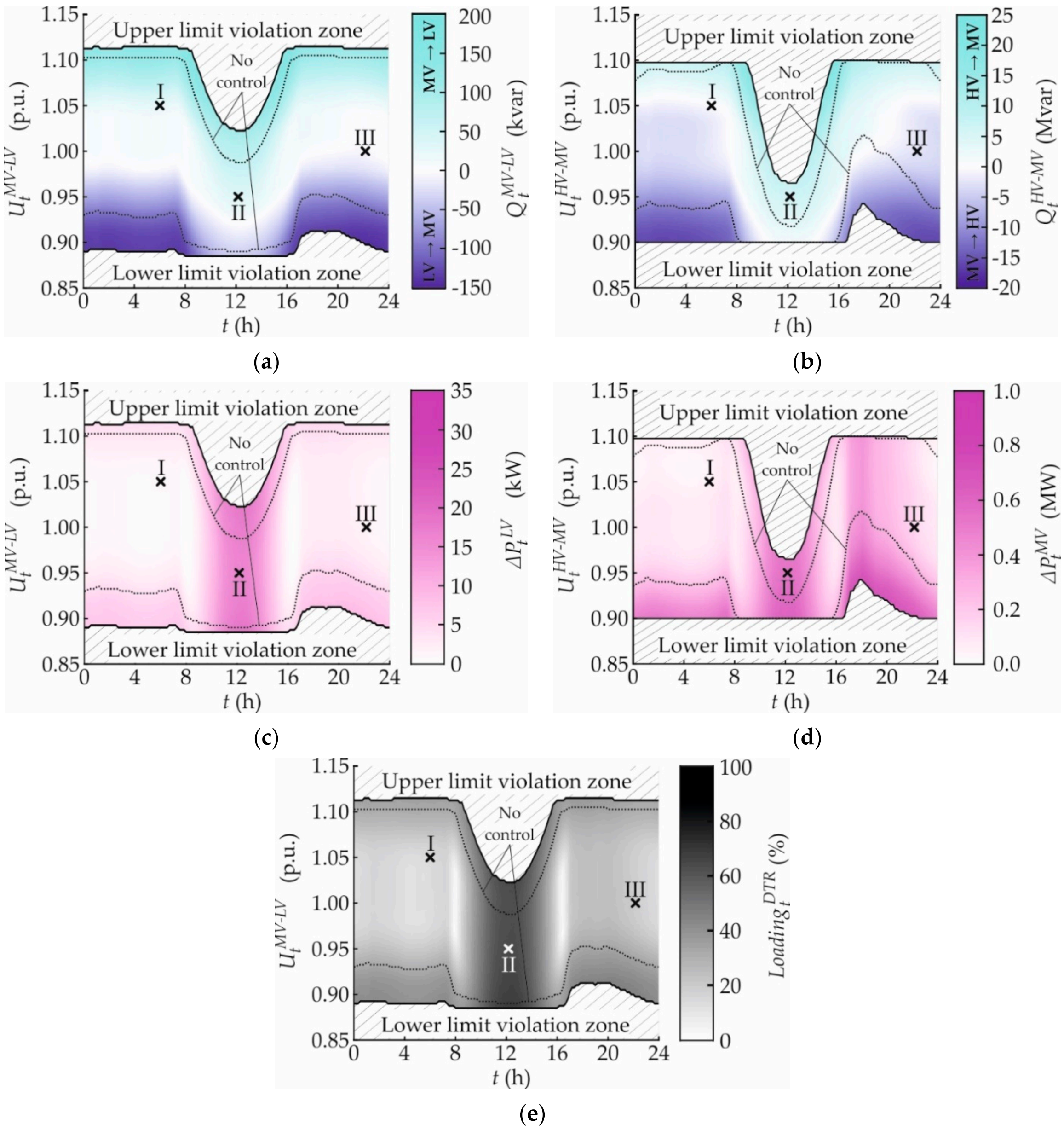

Figure 17. Daily behavior of the test link chain for various boundary voltages and the $Q(U)$ local control: (**a**) reactive power exchange over the MV−LV boundary (rural LV_Link-Grid); (**b**) reactive power exchange over the HV−MV boundary; (**c**) active power loss within the rural LV_Link-Grid; (**d**) active power loss within the MV_Link-Grid; (**e**) DTR loading (rural LV_Link-Grid).

The MV−LV reactive power exchange is considerably intensified in the edge regions of the permissible voltage range (Figure 17a). Although no limit violations occur without any Volt/var control, the reactive power exchange is increased to 26.02, 35.30, and −4.08 kvar in cases I, II, and III, respectively. The HV−MV reactive power exchange, shown in Figure 17b, is modified almost in the complete voltage−time plane. In cases I and II, the MV_Link-Grid draws 0.11 and 6.40 Mvar from the HV level, respectively, while in case III, it injects 2.59 Mvar. In addition, LV losses are increased in the edge regions of the acceptable MV−LV boundary voltage range, provoking 0.83, 16.44, and 1.40 kW in cases I, II, and III, respectively (Figure 17c). At the MV level, $Q(U)$ increases the active power loss for HV−MV boundary voltages close to the lower limit and decreases it for voltages close to the upper limit (Figure 17d). Consequently, the loss is reduced to 52.61 kW in case I and increased to 538.54 and 149.24 kW in cases II and III, respectively. The additional reactive power flows provoked by $Q(U)$ increase the DTR loading (Figure 17e). In cases I, II, and III, the DTR is loaded by 14.82, 64.27, and 18.50%, respectively.

3.2.3. $X(U)$

Figure 18 shows the daily behavior of the test link chain for various boundary voltages and the $X(U)$ local control. $X(U)$ significantly widens the permissible voltage band at both boundaries by adding only small portions of reactive power. The upper and lower $BVL^{MV\text{-}LV}$ are straightened, leaving only small limit protrusions. As a further consequence, the upper $BVL^{HV\text{-}MV}$ is greatly relaxed around midday, and the lower one remains relatively restrictive in the evening hours: voltages up to 1.035 p.u. and down to 0.9775 p.u. are acceptable at midday and 18:00 p.m., respectively.

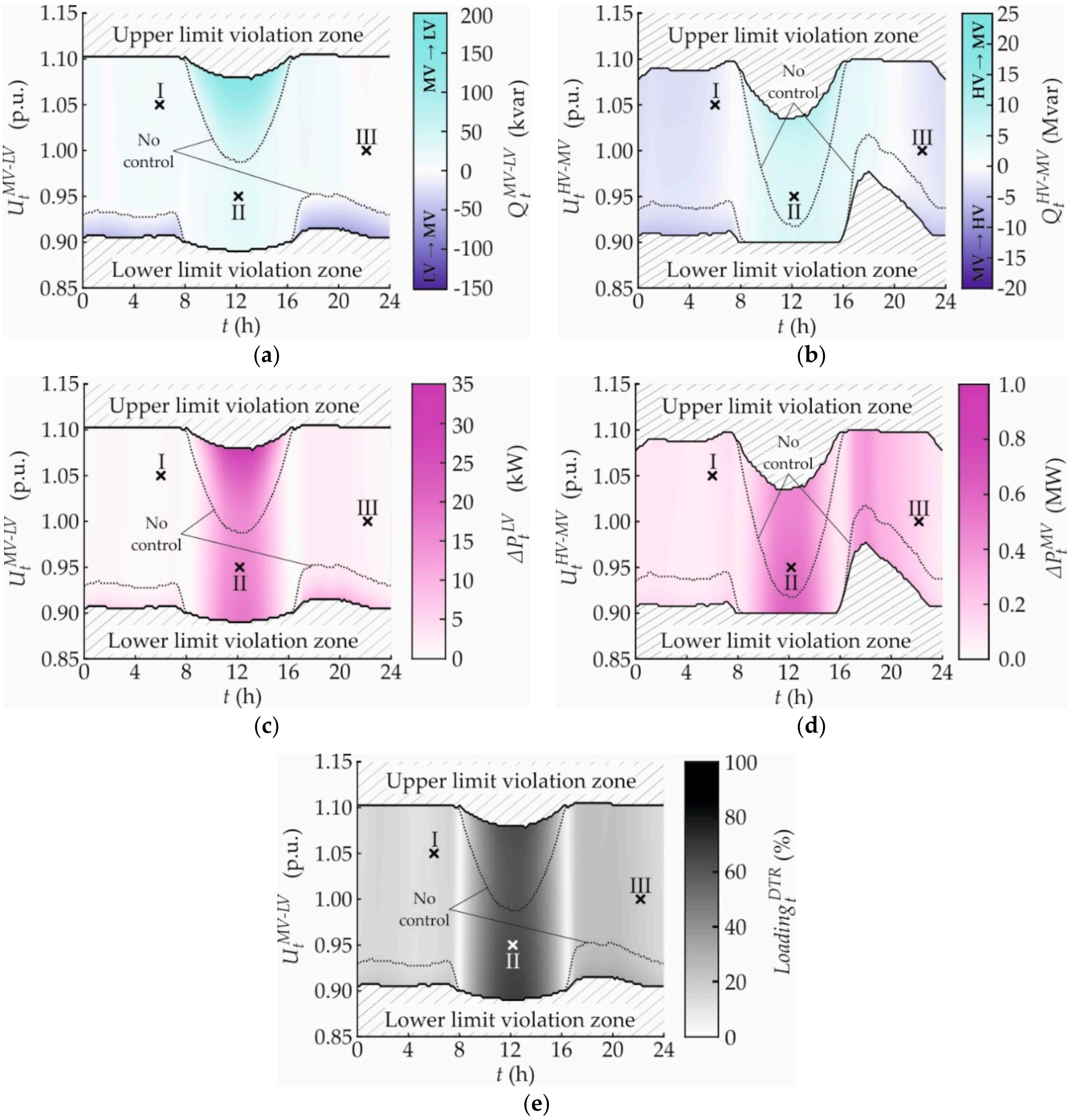

Figure 18. Daily behavior of the test link chain for various boundary voltages and the $X(U)$ local control: (**a**) reactive power exchange over the MV−LV boundary (rural LV_Link-Grid); (**b**) reactive power exchange over the HV−MV boundary; (**c**) active power loss within the rural LV_Link-Grid; (**d**) active power loss within the MV_Link-Grid; (**e**) DTR loading (rural LV_Link-Grid).

$X(U)$ is active mainly in (U,t)-regions where limit violations would occur without any Volt/var control: it is inactive in the selected cases from the viewpoint of the $BLiN^{MV\text{-}LV}$ and active in case II from the perspective of the $BLiN^{HV\text{-}MV}$. Consequently, the MV−LV reactive power exchanges (Figure 18a), LV active power loss (Figure 18c), and DTR loading (Figure 18d) are not affected in cases I, II, and III. Meanwhile, in case II, the reactive power flow through the $BLiN^{HV\text{-}MV}$ is increased to 5.52 Mvar (Figure 18b), modifying the corresponding MV active power loss insignificantly (Figure 18d).

3.2.4. OLTC

Figure 19 shows the daily behavior of the test link chain for various boundary voltages and OLTC local control. OLTC shifts the $BVL^{MV\text{-}LV}$ by around ±5% in parallel, conserving their original shape. Meanwhile, the parallel shifting effect of the $BVL^{HV\text{-}MV}$ is restricted by the fact that the commercial and industrial CP_Link-Grids and the hydroelectric power plants do not include transformers with OLTCs. However, the upper limit is increased during noon-time, and the lower one is decreased in the remaining time intervals. However, both limits remain relatively restrictive: maximal and minimal HV−MV boundary voltages of 0.9725 p.u. are acceptable at midday and 18:00 p.m., respectively.

Figure 19a shows that the MV−LV reactive power exchange is slightly reduced to 10.46 and −2.06 kvar in cases I and III, respectively. In the same cases, 2.23 and 2.27 Mvar flow from the MV into the HV level (Figure 19b). Meanwhile, 5.33 Mvar flows reversely in case II. The OLTC reduces the LV grid loss to 0.76 kW in case I and increases it to 1.418 kW in case III (Figure 19c). Figure 19d shows that MV losses of 81.92, 537.24, and 143.63 kW occur in cases I, II, and III, respectively. Meanwhile, the DTR loading is decreased in cases I and III, obtaining values of 13.05 and 18.21%, respectively (Figure 19e).

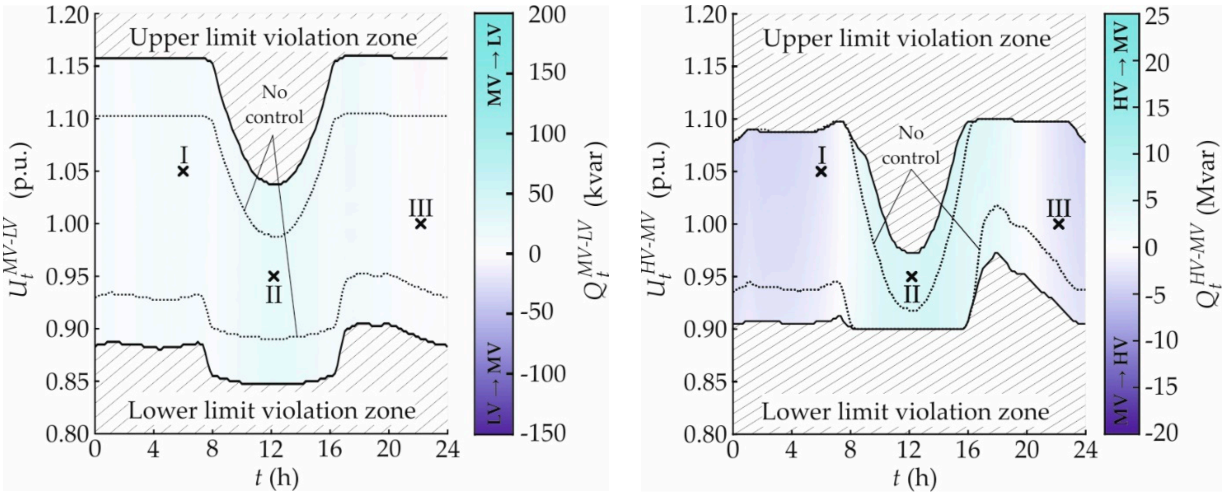

(**a**) (**b**)

Figure 19. *Cont.*

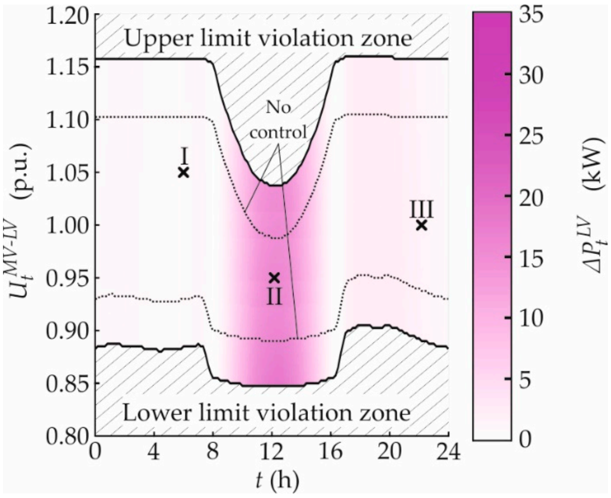

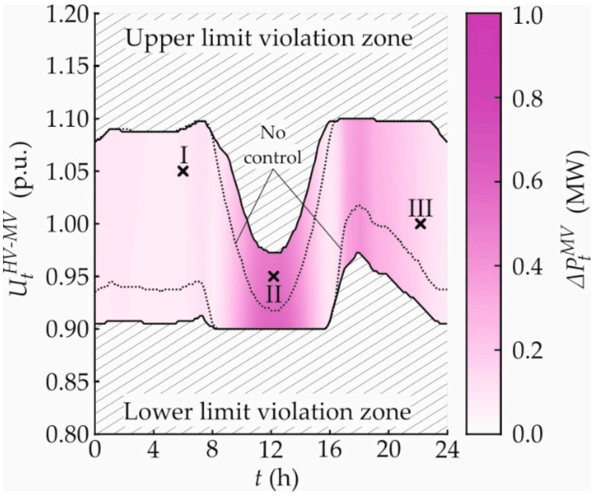

(**c**) (**d**)

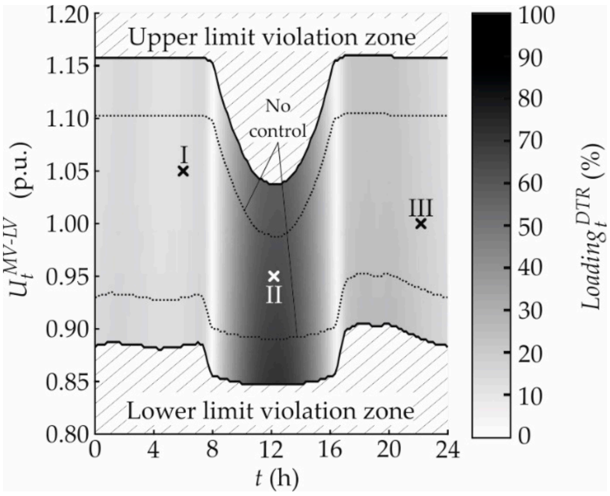

(**e**)

Figure 19. Daily behavior of the test link chain for various boundary voltages and the OLTC local control: (**a**) reactive power exchange over the MV−LV boundary (rural LV_Link-Grid); (**b**) reactive power exchange over the HV−MV boundary; (**c**) active power loss within the rural LV_Link-Grid; (**d**) active power loss within the MV_Link-Grid; (**e**) DTR loading (rural LV_Link-Grid).

3.3. Control Ensembles

3.3.1. *X*(*U*) and CP_*Q*-Autarky

Figure 20 shows the daily behavior of the test link chain for various boundary voltages, the *X*(*U*) local control, and CP_*Q*-Autarky. In combination with the *X*(*U*) local control, CP_*Q*-Autarky has a very low impact on the *BVL*s at both regarded system boundaries: the upper and lower limits are slightly decreased.

Figure 20a shows that the local compensation of the customers' reactive power demand reduces the MV−LV reactive power exchange to 0.52, 15.19, and 1.15 kvar in cases I, II, and III, respectively. As a further consequence, the capacitive behavior seen from the HV level is intensified in cases I and III, reaching 7.48 and 6.58 Mvar, respectively (Figure 20b). In case II, the reactive power flow is reversed: 4.75 Mvar flow into the HV level. The reduced reactive power flows at the LV level reduce the corresponding losses to 0.74, 15.86, and 1.39 kW in cases I, II, and III, respectively (Figure 20c). Meanwhile, Figure 20d shows that the MV losses are increased to 121.45, 554.80, and 181.14 kW, respectively. The DTR is slightly unloaded by the *Q*-Autarky of CPs, reaching 13.51, 63.81, and 18.46% in cases I, II, and III, respectively (Figure 20e).

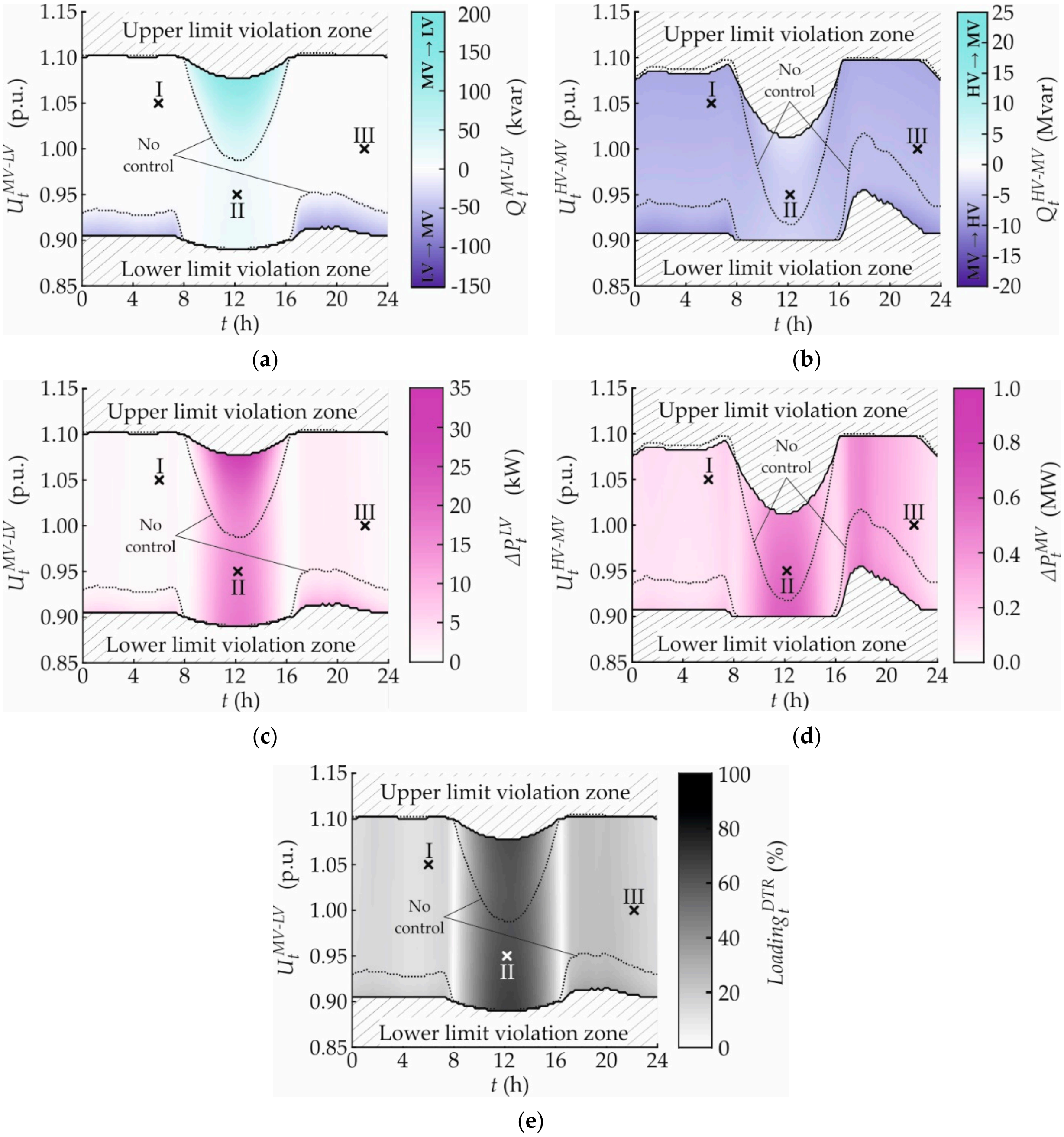

Figure 20. Daily behavior of the test link chain for various boundary voltages, the *X*(*U*) local control, and CP_*Q*-Autarky: (**a**) reactive power exchange over the MV−LV boundary (rural LV_Link-Grid); (**b**) reactive power exchange over the HV−MV boundary; (**c**) active power loss within the rural LV_Link-Grid; (**d**) active power loss within the MV_Link-Grid; (**e**) DTR loading (rural LV_Link-Grid).

3.3.2. OLTC and CP_*Q*-Autarky

Figure 21 shows the daily behavior of the test link chain for various boundary voltages, the OLTC local control, and CP_*Q*-Autarky. In addition, combined with OLTC local control, *Q*-Autarky of CPs slightly reduces the upper and lower *BVL*s at both boundaries.

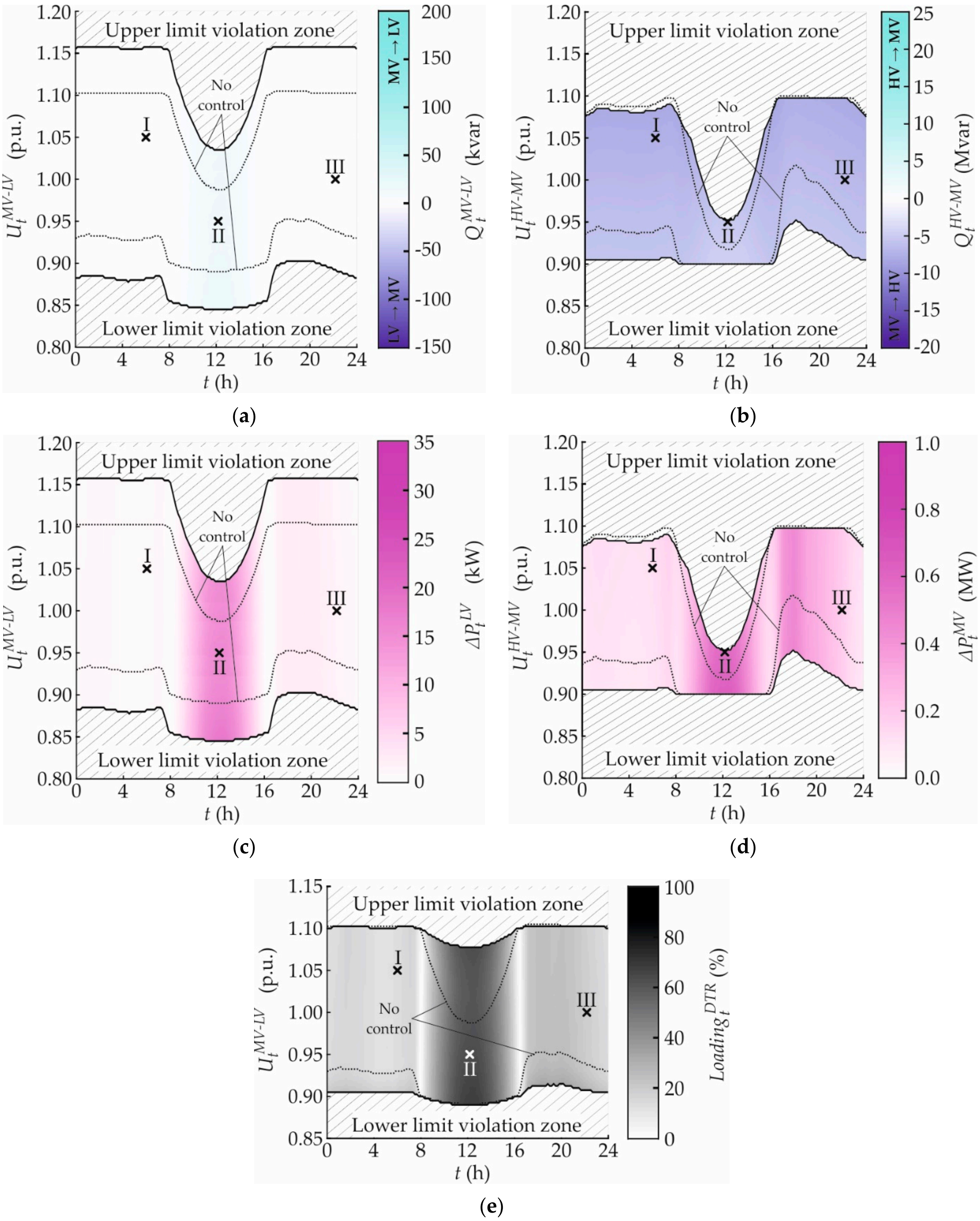

Figure 21. Daily behavior of the test link chain for various boundary voltages, the OLTC local control, and CP_*Q*-Autarky: (**a**) reactive power exchange over the MV−LV boundary (rural LV_Link-Grid); (**b**) reactive power exchange over the HV−MV boundary; (**c**) active power loss within the rural LV_Link-Grid; (**d**) active power loss within the MV_Link-Grid; (**e**) DTR loading (rural LV_Link-Grid).

As shown in Figure 21a, this control ensemble greatly reduces the MV−LV reactive power exchange to 0.54, 15.19, and 1.18 kvar in cases I, II, and III, respectively. Figure 21b shows that the MV grid is capacitive in the complete voltage−time plane, injecting 7.48, 5.14, and 6.58 Mvar into the HV level in cases I, II, and III, respectively. The reduced *Q*-flows at the LV level decrease the corresponding losses to 0.74, 15.86, and 1.416 kW for cases I, II, and III, respectively (Figure 21c). Meanwhile, according to Figure 21d, MV losses are increased to 119.65, 572.32, and 180.34 kWm, respectively. Due to the reduced reactive power flows through the DTR, its loading is decreased to 12.84, 63.81, and 18.20% in cases I, II, and III, respectively (Figure 21e).

4. Comparison of Volt/var Control Arrangements

The investigated control arrangements have different effects on the grid's behavior. Their impact on the boundary voltage limits, reactive power flows, active power losses, and DTR loadings is discussed below.

4.1. Impact on Boundary Voltage Limits

Figure 22 shows the voltage limits at different system boundaries for various control arrangements. Different colors and line types present the various control strategies. The setup without any Volt/var control is indicated by black-colored dotted lines. All control strategies are depicted in solid lines using different colors, as follows: cos*φ*(*P*) in yellow, *Q*(*U*) in orange, *X*(*U*) in green, and OLTC in purple. The combinations of different control strategies are shown by dashed lines in other colors, as follows: *X*(*U*) combined with *Q*-Autarky in lighter shaded green and OLTC combined with *Q*-Autarky in lighter purple.

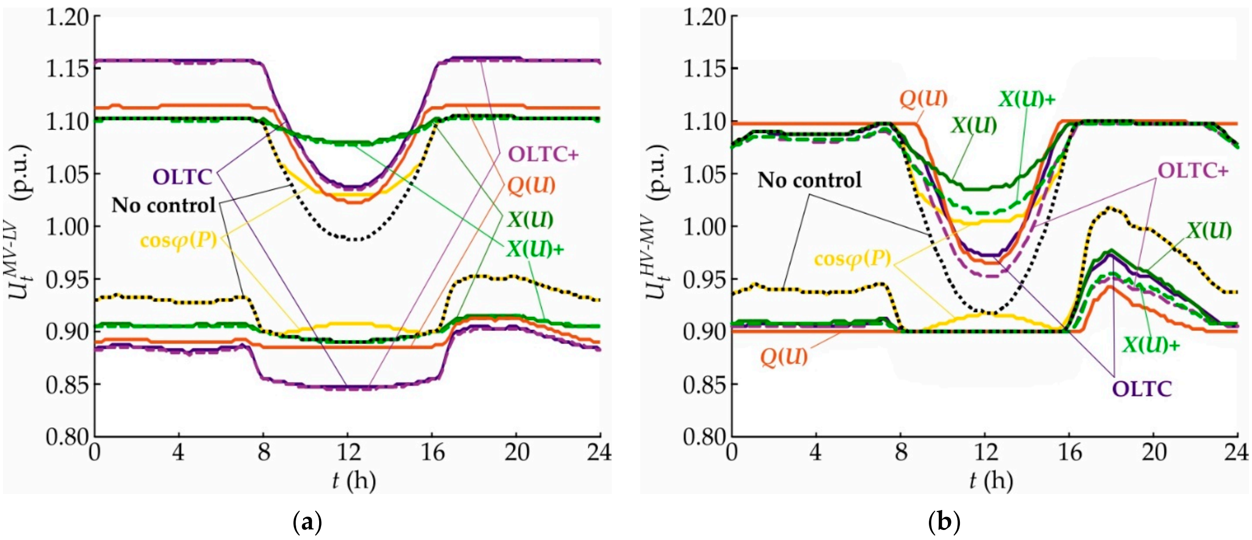

Figure 22. Voltage limits at different system boundaries for various control arrangements: (**a**) MV−LV boundary (rural LV_Link-Grid); (**b**) HV−MV boundary.

Whether combined with CP_*Q*-Autarky or not, the *X*(*U*) local control has the greatest impact on the upper $BVL^{MV\text{-}LV}$ around midday (Figure 22a): it allows for MV−LV boundary voltages up to 1.08 p.u. In contrast, using cos*φ*(*P*), *Q*(*U*), or OLTC local controls severely restricts the upper voltage limit to be respected at the distribution substation. Regarding the lower $BVL^{MV\text{-}LV}$, OLTC shows the best results: the limit remains below 0.905 p.u. throughout the whole day, reaching its maximum value in the early evening hours. In addition, at the $\text{BLiN}^{\text{HV-MV}}$, the *X*(*U*) local control has the most significant impact on the upper *BVL* at noon-time (Figure 22b). The other local controls provoke highly restrictive upper voltage limits to be respected at the supplying substation. Meanwhile, the *Q*(*U*) local control decreases the lower $BVL^{HV\text{-}MV}$ the best, and cos*φ*(*P*) yields unacceptable restrictive limits.

In any case, the *BVL*s are significantly deformed compared with the constant voltage limits stipulated by the Grid Code. The concept of voltage limit distortion (*VLD*) is introduced to evaluate the impact of different control strategies on the time-variability of boundary voltage limits. It is calculated by Equation (10). The larger the *VLD*, the more actions are required during the day to maintain the voltage.

$$VLD_c^{Total} = VLD_c^{MV-LV} + VLD_c^{HV-MV} \quad (10)$$

where c indexes the control arrangement for which the *VLD* is calculated; t_n is the time interval n; $(N-1)$ is the number of simulated time intervals; and $\overline{BVL}^{MV-LV}$, $\overline{BVL}^{HV-MV}$, $\underline{BVL}^{MV-LV}$, and $\underline{BVL}^{HV-MV}$ are the upper and lower MV−LV and HV−MV boundary voltage limits, respectively.

Figure 23 and Table 3 show the *VLD* values for all of the investigated control setups. The grid structure provokes considerable voltage limit distortions of 0.1337% and 0.2370% for the MV−LV and HV−MV boundaries, respectively, and 0.3707% in total. All Volt/var control arrangements decrease the *VLD*, except the OLTC local control (whether combined with CP_*Q*-Autarky or not), which slightly increases the $VLD^{MV\text{-}LV}$. The *X*(*U*) local control yields the lowest $VLD^{MV\text{-}LV}$ for all control setups, while the OLTC in distribution substation provokes the highest one. The lowest limit distortion occurs at the $BLiN^{HV\text{-}MV}$ when the *X*(*U*) local control is combined with CP_*Q*-Autarky, and the highest one when OLTC is used. The lowest total *VLD* in the chain provokes the control ensemble: *X*(*U*) combined with CP_*Q*-Autarky.

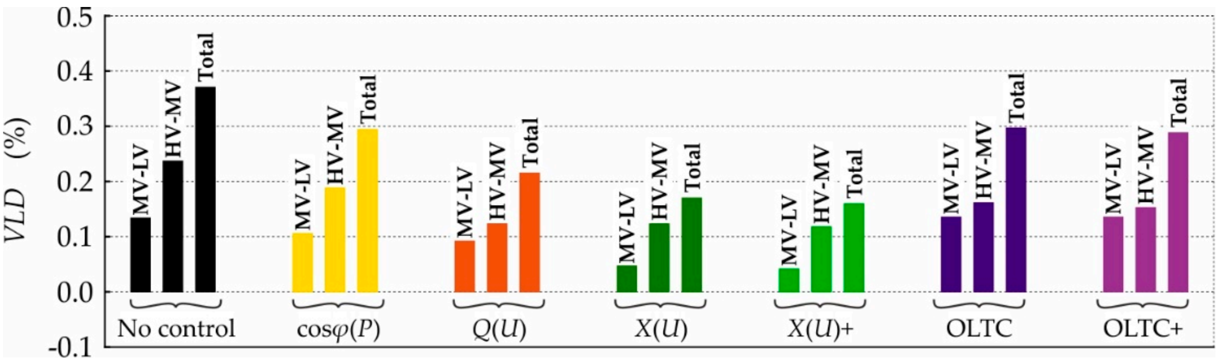

Figure 23. Voltage limit distortion for various control arrangements.

Table 3. Voltage limit distortion for various control arrangements.

Volt/var Control Arrangement	Voltage Limit Distortion		
	MV−LV Boundary	HV−MV Boundary	Total
No control	0.1337%	0.2370%	0.3707%
cosφ(*P*) local control	0.1059%	0.1884%	0.2943%
Q(*U*) local control	0.0920%	0.1233%	0.2153%
X(*U*) local control	0.0469%	0.1233%	0.1702%
X(*U*) local control and CP_*Q*-Autarky	0.0417%	0.1181%	0.1598%
OLTC local control	0.1354%	0.1528%	0.2882%
OLTC local control and CP_*Q*-Autarky	0.1354%	0.1615%	0.2969%

4.2. Impact on Reactive Power Flows

Figure 24 shows the composition of the reactive power exchanged for different control strategies and cases. The reactive power crossing the MV−LV boundary, shown in Figure 24a, consists of two components: the *Q*-amount of CP_Link-Grids, which is determined by the corresponding consuming devices and PV systems, and the *Q*-amount of the LV_Link-Grid itself, which represents the reactive power contributions of the LV lines, DTR, and RPDs (only relevant when the *X*(*U*) local control is used). Significant *Q*-amounts of the

LV_Link-Grid are found only in case II, where relatively high reactive power losses occur. The cos$\varphi(P)$ local control drastically increases the CPs' reactive power consumptions in case II, causing additional reactive power losses as a further consequence. $Q(U)$ intensifies the LV−CP reactive power exchanges in all cases. Due to its inactivity in the selected cases, the $X(U)$ local control does not modify the corresponding reactive power compositions. In cases I and III, the OLTC reduces the CPs' Q-amounts while increasing the reactive power losses at the LV level. With both control ensembles, Q-Autarkic customers do not exchange any reactive power with the grid, reducing the grid's reactive power loss.

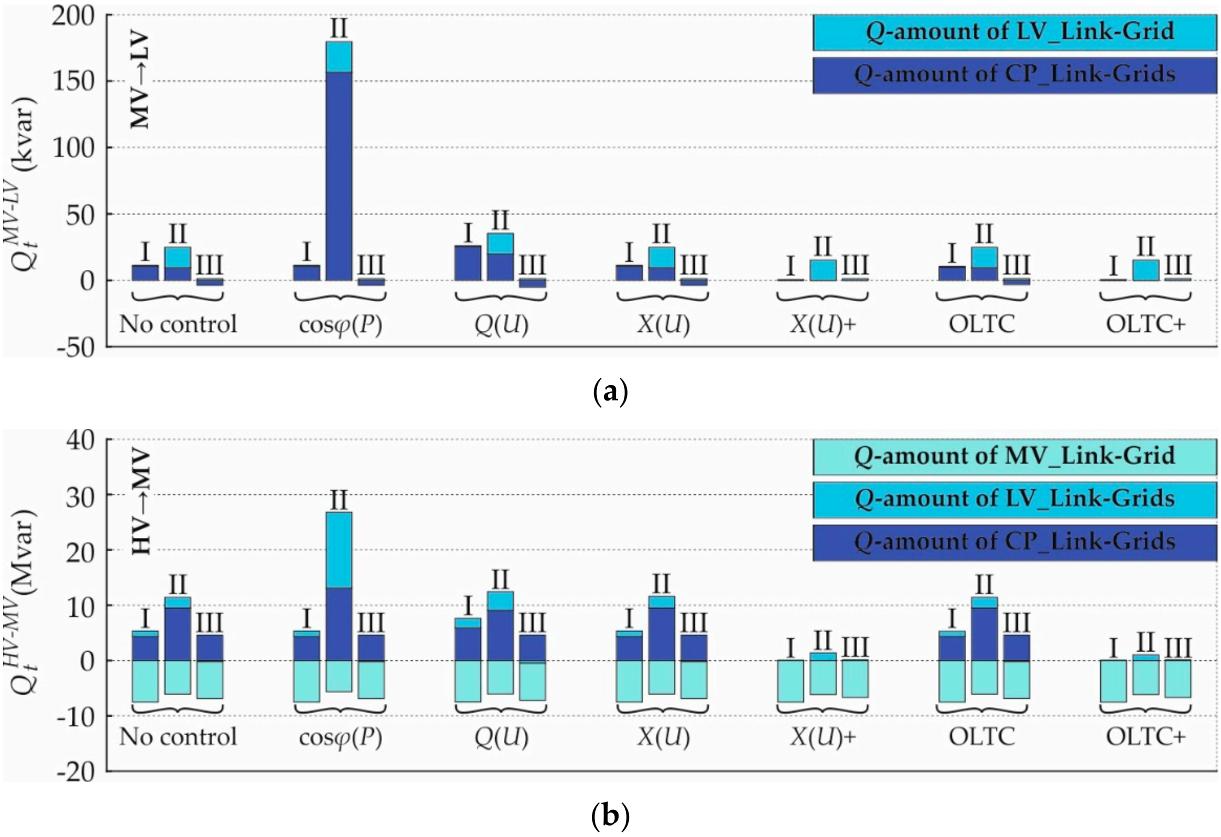

Figure 24. Composition of the reactive power exchange for various control strategies and cases in different system boundaries: (**a**) MV−LV; (**b**) HV−MV.

The MV_Link-Grid connects CP and LV_Link-Grids and hydroelectric power plants. Therefore, the reactive power flow through the BLiN$^{HV\text{-}MV}$, shown in Figure 24b, contains Q-amounts of three different components: commercial and industrial CP_Link-Grids, urban and rural LV_Link-Grids, and the MV_Link-Grid itself. The hydroelectric power plants do not contribute any reactive power. Due to its high cable share, the MV_Link-Grid generally produces significant amounts of reactive power. Especially in case II, this reactive power production is partly compensated by the reactive power losses in the MV lines' series impedances. Non-Q-Autarkic CPs consume substantial amounts of reactive power for all of the control arrangements. This Q-consumption is significantly intensified by the cos$\varphi(P)$ local control in case II and by $Q(U)$ in case I. Furthermore, the $Q(U)$ and especially cos$\varphi(P)$ local controls considerably increase the reactive power consumption of LV_Link-Grids, as they enlarge the Q-consumption of the thereto connected residential CPs. Meanwhile, the $X(U)$ and OLTC local controls have low impacts on the Q-composition at the BLiN$^{HV\text{-}MV}$. In any combination, CP_Q-Autarky eliminates the reactive power contributions of CPs and reduces the ones of the LV_Link-Grids.

4.3. Impact on Active Power Losses

Figure 25 depicts the active power loss for various control strategies and cases. High losses occur within the rural LV_Link-Grid in case II for each control strategy, while relatively low ones prevail in cases I and III (Figure 25a). The cos$\varphi(P)$ local control considerably intensifies the grid losses in case II. Meanwhile, $Q(U)$ slightly increases the losses in all cases. $X(U)$ does not affect the losses in any of the selected cases. When an OLTC is used, the losses are decreased in case I and increased in case III. The application of CP_Q-Autarky generally reduces the LV grid loss.

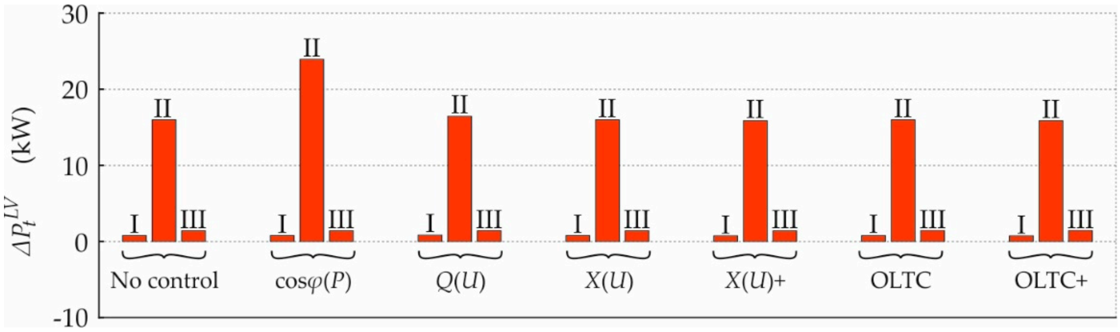

(**a**)

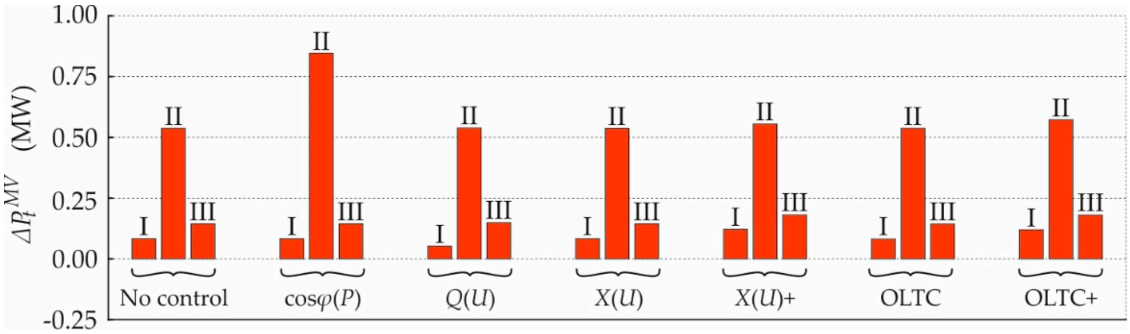

(**b**)

Figure 25. Active power loss for various control strategies and cases within different system levels: (**a**) LV level (rural LV_Link-Grid); (**b**) MV level.

Due to the intensive power transfer, relatively high losses prevail at the MV level in case II, while lower ones occur in case III and especially in case I (Figure 25b). The cos$\varphi(P)$ local control considerably intensifies the loss in case II, as it drastically increases the reactive power flows through the MV lines. Meanwhile, $Q(U)$ partly compensates for the reactive power production of the MV lines in case I, thus reducing the reactive power flows at the MV level and the associated active power loss. Both the $X(U)$ and OLTC local controls do not significantly affect the losses in all cases. Their combinations with CP_Q-Autarky increase the MV reactive power flows and thus the corresponding active power loss.

4.4. Impact on Distribution Transformer Loadings

Figure 26 shows the DTR loading within the rural LV_Link-Grid for different cases, no control, and various control strategies. Compared with the cos$\varphi(P)$ local control, which drastically increases the DTR loading in case II, the other control strategies have a marginal impact. In contrast with the $X(U)$ local control, $Q(U)$ slightly increases the DTR loading in all cases. Using an OLTC reduces the DTR loading in cases I and III. In any combination, Q-Autarkic CPs unload the DTR from their reactive power contributions.

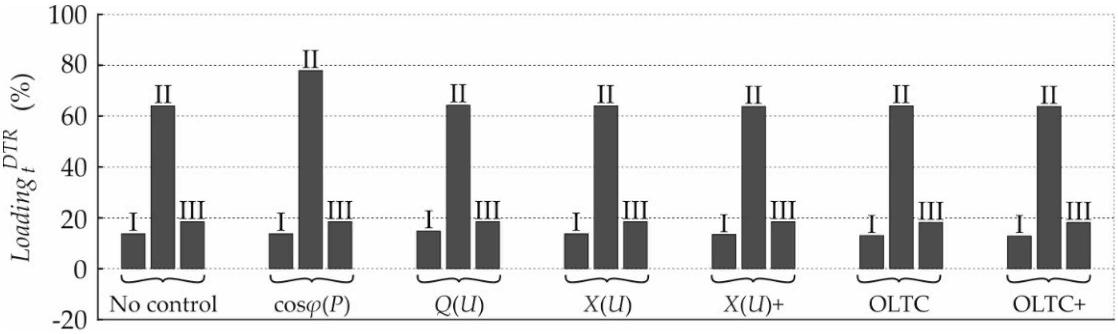

Figure 26. DTR loading within the rural LV_Link-Grid for different cases, no control, and various control strategies.

The above analysis shows that $X(U)$ and its combination with Q-Autarkic CPs have distinct advantages compared with the other control strategies. All of the studied control strategies are applied at the LV and CP levels. The consideration of the Vv$\mathbf{SC}^{\mathrm{MV}}$ and reactive power support from RPDs, storages, and producers connected at the MV level will be necessary to control the reactive power flow at the HV−MV boundary, which is of the utmost importance for DSOs and TSOs. The latter is beyond the scope of this paper, constituting an important field of future research.

5. Conclusions

The increasing distributed generation and electricity demand challenges the Volt/var control process to maintain voltage limit compliance at the customers' delivery points. Simulations show that the control ensemble $X(U)$ local control combined with Q-Autarkic customer plants performs better than the cos$\varphi(P)$ and $Q(U)$ local control strategies applied on photovoltaic inverters and the on-load tap changers in distribution substations. It provokes the lowest voltage limit distortion, requiring the least amount of action to maintain the voltage throughout the day. It sufficiently widens the upper voltage limits to be respected at the distribution and supplying substations around midday. Consequently, voltage limit violations at the customers' delivery points are eliminated, provoking relatively low reactive power exchanges between the medium and low voltage grids, lower losses, and lower distribution transformer loading.

Author Contributions: Conceptualization, D.-L.S. and A.I.; methodology, D.-L.S.; software, D.-L.S.; formal analysis, D.-L.S.; investigation, D.-L.S.; writing—original draft preparation, D.-L.S.; writing—review and editing, A.I.; visualization, D.-L.S.; supervision, A.I. All authors have read and agreed to the published version of the manuscript.

Funding: Open Access Funding by TU Wien.

Data Availability Statement: Data are contained within the article.

Conflicts of Interest: The authors declare no conflict of interest.

Appendix A

- Primary control refers to control actions executed locally in a closed-loop: The input and output variables are the same. The output or control variable is locally measured and continuously compared with the set-point received from the corresponding SC. The deviation from the set-point results in a signal that influences the valves or frequency, excitation current or reactive power, transformer tap positions, etc., in a primary-controlled power plant, transformer, and so on, such that the desired power is delivered or the desired voltage is reached.
- Direct control refers to control actions performed locally in an open-loop, taking into account the holistic real-time behavior of the corresponding grid part. The secondary control calculates the corresponding control action, e.g., changing a circuit breaker's switch position.

- Secondary control refers to control variables that are calculated based on the current state of a control area. It fulfills a predefined objective function by respecting static and dynamic constraints (P/Q capabilities of generators, transformer and line rating, voltage limits, reactive power limits, etc.). It calculates and sends the set-points to PCs and the input variables DiCs acting on its area.
- Local control refers to control actions that are carried out locally without considering the holistic real-time behavior of the relevant grid part. Its action path may be realized in an open- or closed-loop. LC automatically adjusts the active/reactive power contributions of RPDs, storages, and producers and the tap positions of transformers based on local measurements or time schedules [21,45,46]. It usually maintains a power system parameter, which is locally measured or calculated based on local measurements, equal to the desired value. The fixed control settings are calculated based on offline system analysis for typical operating conditions. LCs are simple, reliable, and respond quickly to changing operating conditions without the need for a communication infrastructure [47–49].

Appendix B

The models of the urban residential, commercial, and industrial CP_Link-Grids are presented below.

- Urban residential CP_Link-Grid

This CP type is connected to the urban LV_Link-Grid. It has the same structure and profiles as the rural residential one (see Figure 5a), except for one detail: the Dev.-model's load profiles are increased by the factor 1.43.

- Commercial CP_Link-Grid

This CP type has the same structure as the residential ones (see Figure 4b): a single node connects the Dev.-, Pr.-, and St.-models. The load profiles [50] shown in Figure A1a and the time-varying ZIP-coefficients from [51] determine the Dev.-model's behavior. The Pr.-model represents the PV system: it has module and inverter ratings of 50 kW and 55.56 kVA, respectively. The profile shown in Figure A1b specifies the P-injection of the Pr.-model, and its Q-contribution depends on the applied Volt/var control strategy. The St.-model represents the EV batteries that are connected to the CP_Link-Grid through three EV chargers. Their P-behavior is determined by ZIP-coefficients [40] and load profiles [41] (Figure A1c). No reactive power is absorbed or injected.

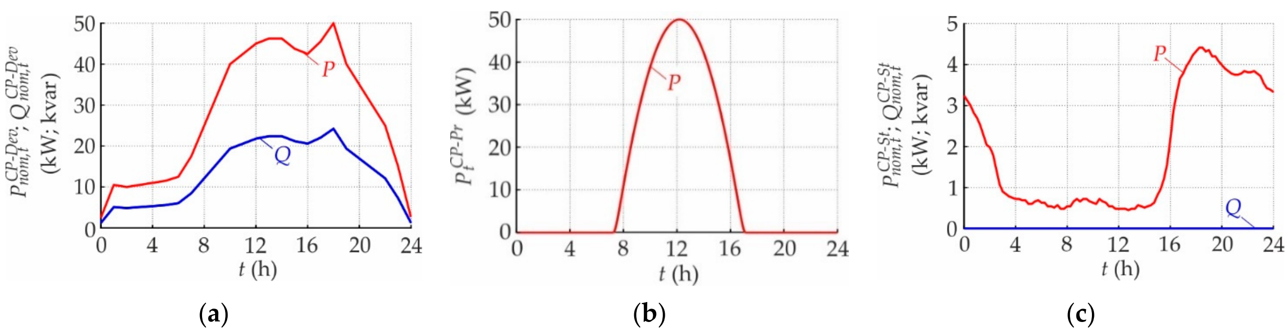

Figure A1. Load and production profiles of different model components of the commercial CP_Link-Grid: (**a**) Dev.-model; (**b**) Pr.-model; (**c**) St.-model.

- Industrial CP

The industrial CP_Link-Grid does not include the St.-model (Figure A2a). The load profiles [50] and constant ZIP-coefficients [51] determine the Dev.-model's behavior (Figure A2b). The PV system is represented by the Pr.-model and has module and inverter ratings of 300 kW and 333.33 kVA, respectively. Its P-injection follows the profile shown in

Figure A2c, and its reactive power contribution depends on the applied Volt/var control strategy. In the case of CP_Q-Autarky, an additional (lossless) RPD is added to enable the full compensation of the reactive power flow through the BLiN$^{MV\text{-}CP}$.

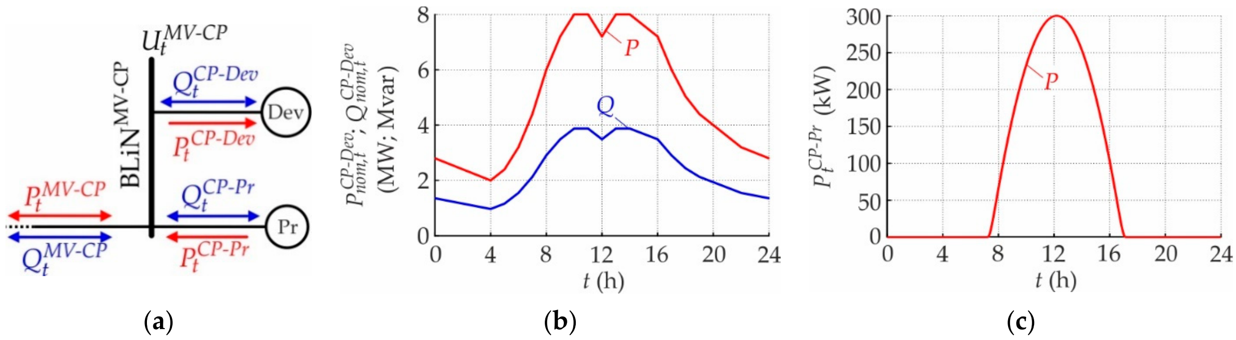

Figure A2. Industrial CP_Link-Grid: (**a**) structure; (**b**) load profiles of the Dev.-model; (**c**) production profile of the Pr.-model.

References

1. Lopes, J.A.P.; Hatziargyriou, N.; Mutale, J.; Djapic, P.; Jenkins, N. Integrating Distributed Generation into Electric Power Systems: A Review of Drivers, Challenges and Opportunities. *Electr. Power Syst. Res.* **2007**, *77*, 1189–1203. [CrossRef]
2. Bollen, M.H.J.; Sannino, A. Voltage Control with Inverter-Based Distributed Generation. *IEEE Trans. Power Deliv.* **2005**, *20*, 519–520. [CrossRef]
3. Bletterie, B.; Kadam, S.; Bolgaryn, R.; Zegers, A. Voltage Control with PV Inverters in Low Voltage Networks—In Depth Analysis of Different Concepts and Parameterization Criteria. *IEEE Trans. Power Syst.* **2017**, *32*, 177–185. [CrossRef]
4. Demirok, E.; González, P.C.; Frederiksen, K.H.B.; Sera, D.; Rodriguez, P.; Teodorescu, R. Local Reactive Power Control Methods for Overvoltage Prevention of Distributed Solar Inverters in Low-Voltage Grids. *IEEE J. Photovolt.* **2011**, *1*, 174–182. [CrossRef]
5. Turitsyn, K.; Sulc, P.; Backhaus, S.; Chertkov, M. Options for Control of Reactive Power by Distributed Photovoltaic Generators. *Proc. IEEE* **2011**, *99*, 1063–1073. [CrossRef]
6. Karthikeyan, N.; Pokhrel, B.R.; Pillai, J.R.; Bak-Jensen, B. Coordinated Voltage Control of Distributed PV Inverters for Voltage Regulation in Low Voltage Distribution Networks. In Proceedings of the 2017 IEEE PES Innovative Smart Grid Technologies Conference Europe (ISGT-Europe), Turin, Italy, 26–29 September 2017; pp. 1–6.
7. Smith, J.W.; Sunderman, W.; Dugan, R.; Seal, B. Smart Inverter Volt/Var Control Functions for High Penetration of PV on Distribution Systems. In Proceedings of the 2011 IEEE/PES Power Systems Conference and Exposition, Phoenix, AZ, USA, 20–23 March 2011; pp. 1–6.
8. Zhang, F.; Guo, X.; Chang, X.; Fan, G.; Chen, L.; Wang, Q.; Tang, Y.; Dai, J. The Reactive Power Voltage Control Strategy of PV Systems in Low-Voltage String Lines. In Proceedings of the 2017 IEEE Manchester PowerTech, Manchester, UK, 18–22 June 2017; pp. 1–6.
9. Wang, J.; Bharati, G.R.; Paudyal, S.; Ceylan, O.; Bhattarai, B.P.; Myers, K.S. Coordinated Electric Vehicle Charging With Reactive Power Support to Distribution Grids. *IEEE Trans. Ind. Inform.* **2019**, *15*, 54–63. [CrossRef]
10. Leemput, N.; Geth, F.; Van Roy, J.; Büscher, J.; Driesen, J. Reactive Power Support in Residential LV Distribution Grids through Electric Vehicle Charging. *Sustain. Energy Grids Netw.* **2015**, *3*, 24–35. [CrossRef]
11. Ilo, A.; Schultis, D.-L.; Schirmer, C. Effectiveness of Distributed vs. Concentrated Volt/Var Local Control Strategies in Low-Voltage Grids. *Appl. Sci.* **2018**, *8*, 1382. [CrossRef]
12. Stetz, T.; Marten, F.; Braun, M. Improved Low Voltage Grid-Integration of Photovoltaic Systems in Germany. *IEEE Trans. Sustain. Energy* **2013**, *4*, 534–542. [CrossRef]
13. Schultis, D.-L.; Ilo, A.; Schirmer, C. Overall Performance Evaluation of Reactive Power Control Strategies in Low Voltage Grids with High Prosumer Share. *Electr. Power Syst. Res.* **2019**, *168*, 336–349. [CrossRef]
14. EU. *Regulation (EU) 2016/679 of the European Parliament and of the Council of 27 April 2016 on the Protection of Natural Persons with Regard to the Processing of Personal Data and on the Free Movement of Such Data, and Repealing Directive 95/46/EC (General Data Protection Regulation) (Text with EEA Relevance)*; EU: Maastricht, The Netherlands, 2016.
15. EU. *Directive (EU) 2019/944 of the European Parliament and of the Council of 5 June 2019 on Common Rules for the Internal Market for Electricity and Amending Directive 2012/27/EU (Text with EEA Relevance.)*; EU: Maastricht, The Netherlands, 2019.
16. Reese, C.; Buchhagen, C.; Hofmann, L. Voltage Range as Control Input for OLTC-Equipped Distribution Transformers. In Proceedings of the PES T&D 2012, Orlando, FL, USA, 7–10 May 2012; pp. 1–6.
17. Hossain, M.I.; Yan, R.; Saha, T. Investigation of the Interaction between Step Voltage Regulators and Large-Scale Photovoltaic Systems Regarding Voltage Regulation and Unbalance. *IET Renew. Power Gener.* **2016**, *10*, 299–309. [CrossRef]
18. Ilo, A.; Schultis, D.-L. Low-Voltage Grid Behaviour in the Presence of Concentrated Var-Sinks and Var-Compensated Customers. *Electr. Power Syst. Res.* **2019**, *171*, 54–65. [CrossRef]

19. Ostergaard, J.; Ziras, C.; Bindner, H.W.; Kazempour, J.; Marinelli, M.; Markussen, P.; Rosted, S.H.; Christensen, J.S. Energy Security Through Demand-Side Flexibility: The Case of Denmark. *IEEE Power Energy Mag.* **2021**, *19*, 46–55. [CrossRef]
20. Chiang, H.-D.; Wang, J.-C.; Tong, J.; Darling, G. Optimal Capacitor Placement, Replacement and Control in Large-Scale Unbalanced Distribution Systems: Modeling and a New Formulation. *IEEE Trans. Power Syst.* **1995**, *10*, 356–362. [CrossRef]
21. Guo, Q.; Qi, J.; Ajjarapu, V.; Bravo, R.; Chow, J.; Li, Z.; Moghe, R.; Nasr-Azadani, E.; Tamrakar, U.; Taranto, G.N.; et al. Review of Challenges and Research Opportunities for Voltage Control in Smart Grids. *IEEE Trans. Power Syst.* **2019**, *34*, 2790–2801. [CrossRef]
22. Lund, P. The Danish Cell Project—Part 1: Background and General Approach. In Proceedings of the 2007 IEEE Power Engineering Society General Meeting, Tampa, FL, USA, 24–28 June 2007. [CrossRef]
23. European Distribution System Operators for Smart Grids—Data Management: The Role of Distribution System Operators in Managing Data. Available online: https://www.edsoforsmartgrids.eu/wp-content/uploads/public/EDSO-views-on-Data-Management-June-2014.pdf (accessed on 27 August 2021).
24. Myrda, P.; Mcgranaghan, M. Smart Grid Enabled Asset Management. In Proceedings of the CIRED Workshop, Lyon, France, 7–8 June 2010; pp. 1–4.
25. Cárdenas, A.A.; Safavi-Naini, R. Chapter 25—Security and Privacy in the Smart Grid. In *Handbook on Securing Cyber-Physical Critical Infrastructure*; Das, S.K., Kant, K., Zhang, N., Eds.; Morgan Kaufmann: Boston, MA, USA, 2012; pp. 637–654. ISBN 978-0-12-415815-3.
26. Vaahedi, E. *Practical Power System Operation*, 1st ed.; John Wiley & Sons, Ltd.: Hoboken, NJ, USA, 2014.
27. O'Connell, N.; Pinson, P.; Madsen, H.; O'Malley, M. Benefits and Challenges of Electrical Demand Response: A Critical Review. *Renew. Sustain. Energy Rev.* **2014**, *39*, 686–699. [CrossRef]
28. Ilo, A. "Link"—The Smart Grid Paradigm for a Secure Decentralized Operation Architecture. *Electr. Power Syst. Res.* **2016**, *131*, 116–125. [CrossRef]
29. Schultis, D.-L.; Ilo, A. Behaviour of Distribution Grids with the Highest PV Share Using the Volt/Var Control Chain Strategy. *Energies* **2019**, *12*, 3865. [CrossRef]
30. Ilo, A. The Energy Supply Chain Net. *Energy Power Eng.* **2013**, *5*, 384–390. [CrossRef]
31. Luo, K.; Shi, W. Comparison of Voltage Control by Inverters for Improving the PV Penetration in Low Voltage Networks. *IEEE Access* **2020**, *8*, 161488–161497. [CrossRef]
32. Almeida, D.; Pasupuleti, J.; Ekanayake, J. Comparison of Reactive Power Control Techniques for Solar PV Inverters to Mitigate Voltage Rise in Low-Voltage Grids. *Electronics* **2021**, *10*, 1569. [CrossRef]
33. Chathurangi, D.; Jayatunga, U.; Perera, S.; Agalgaonkar, A.P.; Siyambalapitiya, T. Comparative Evaluation of Solar PV Hosting Capacity Enhancement Using Volt-VAr and Volt-Watt Control Strategies. *Renew. Energy* **2021**, *177*, 1063–1075. [CrossRef]
34. Schultis, D.-L. Comparison of Local Volt/Var Control Strategies for PV Hosting Capacity Enhancement of Low Voltage Feeders. *Energies* **2019**, *12*, 1560. [CrossRef]
35. Schultis, D.-L.; Ilo, A. Increasing the Utilization of Existing Infrastructures by Using the Newly Introduced Boundary Voltage Limits. *Energies* **2021**, *14*, 5106. [CrossRef]
36. *DIN EN 50160:2020-11, Merkmale Der Spannung in Öffentlichen Elektrizitätsversorgungsnetzen; Deutsche Fassung EN_50160:2010_+ Cor.: 2010_+ A1:2015_+ A2:2019_+ A3:2019*; Beuth Verlag GmbH: Berlin, Germany, 2020.
37. Schultis, D.-L. *Daily Load Profiles and ZIP Models of Current and New Residential Customers*; Data Archiving and Networked Services (DANS): Den Haag, The Netherlands, 2019; Volume 1. [CrossRef]
38. Schultis, D.-L.; Ilo, A. Adaption of the Current Load Model to Consider Residential Customers Having Turned to LED Lighting. In Proceedings of the 2019 IEEE PES Asia-Pacific Power and Energy Engineering Conference (APPEEC), Macao, China, 1–4 December 2019; pp. 1–5.
39. Wang, Y.-B.; Wu, C.-S.; Liao, H.; Xu, H.-H. Steady-State Model and Power Flow Analysis of Grid-Connected Photovoltaic Power System. In Proceedings of the 2008 IEEE International Conference on Industrial Technology, Chengdu, China, 21–24 April 2008; pp. 1–6.
40. Shukla, A.; Verma, K.; Kumar, R. Multi-Stage Voltage Dependent Load Modelling of Fast Charging Electric Vehicle. In Proceedings of the 2017 6th International Conference on Computer Applications In Electrical Engineering-Recent Advances (CERA), Roorkee, India, 5–7 October 2017; pp. 86–91.
41. Aunedi, M.; Woolf, M.; Strbac, G.; Babalola, O.; Clark, M. Characteristic Demand Profiles of Residential and Commercial EV Users and Opportunities for Smart Charging. In Proceedings of the 23rd International Conference on Electricity Distribution (CIRED 2015), Lyon, France, 15–18 June 2015; pp. 1–5.
42. Schultis, D.-L.; Ilo, A. *TUWien_LV_TestGrids*; Mendeley Data: London, UK, 2018; Volume 1. [CrossRef]
43. Technische und Organisatorische Regeln für Betreiber und Benutzer von Netzen. TOR Erzeuger: Anschluss und Parallelbetrieb von Stromerzeugungsanlagen des Typs A und von Kleinsterzeugungsanlagen. Available online: https://www.e-control.at/documents/1785851/1811582/TOR+Erzeuger+Typ+A+V1.0.pdf/6342d021-a5ce-3809-2ae5-28b78e26f04d?t=1562757767659 (accessed on 27 July 2021).
44. Marggraf, O.; Laudahn, S.; Engel, B.; Lindner, M.; Aigner, C.; Witzmann, R.; Schoeneberger, M.; Patzack, S.; Vennegeerts, H.; Cremer, M.; et al. U-Control-Analysis of Distributed and Automated Voltage Control in Current and Future Distribution Grids. In Proceedings of the International ETG Congress 2017, Bonn, Germany, 28–29 November 2017; pp. 1–6.

45. Roytelman, I.; Ganesan, V. Modeling of Local Controllers in Distribution Network Applications. In Proceedings of the 21st International Conference on Power Industry Computer Applications. Connecting Utilities. PICA 99. To the Millennium and Beyond (Cat. No.99CH36351), Santa Clara, CA, USA, 21 May 1999; pp. 161–166.
46. Farivar, M.; Zho, X.; Chen, L. Local Voltage Control in Distribution Systems: An Incremental Control Algorithm. In Proceedings of the 2015 IEEE International Conference on Smart Grid Communications (SmartGridComm), Miami, FL, USA, 2–5 November 2015; pp. 732–737.
47. Nowak, S.; Wang, L.; Metcalfe, M.S. Two-Level Centralized and Local Voltage Control in Distribution Systems Mitigating Effects of Highly Intermittent Renewable Generation. *Int. J. Electr. Power Energy Syst.* **2020**, *119*, 105858. [CrossRef]
48. Zhou, X.; Chen, L.; Farivar, M.; Liu, Z.; Low, S. Reverse and Forward Engineering of Local Voltage Control in Distribution Networks. *IEEE Trans. Autom. Control* **2020**, *66*, 1116–1128. [CrossRef]
49. Roytelman, I.; Ganesan, V. Coordinated Local and Centralized Control in Distribution Management Systems. *IEEE Trans. Power Deliv.* **2000**, *15*, 718–724. [CrossRef]
50. Benchmark Systems for Network Integration of Renewable and Distributed Energy Resources. Available online: https://e-cigre.org/publication/ELT_273_8-benchmark-systems-for-network-integration-of-renewable-and-distributed-energy-resources (accessed on 26 July 2021).
51. Bokhari, A.; Alkan, A.; Dogan, R.; Diaz-Aguiló, M.; de León, F.; Czarkowski, D.; Zabar, Z.; Birenbaum, L.; Noel, A.; Uosef, R.E. Experimental Determination of the ZIP Coefficients for Modern Residential, Commercial, and Industrial Loads. *IEEE Trans. Power Deliv.* **2014**, *29*, 1372–1381. [CrossRef]